Karlsruhe Institute of Technology

ANKA Annual Report 2010

ANKA SYNCHROTRON RADIATION FACILITY

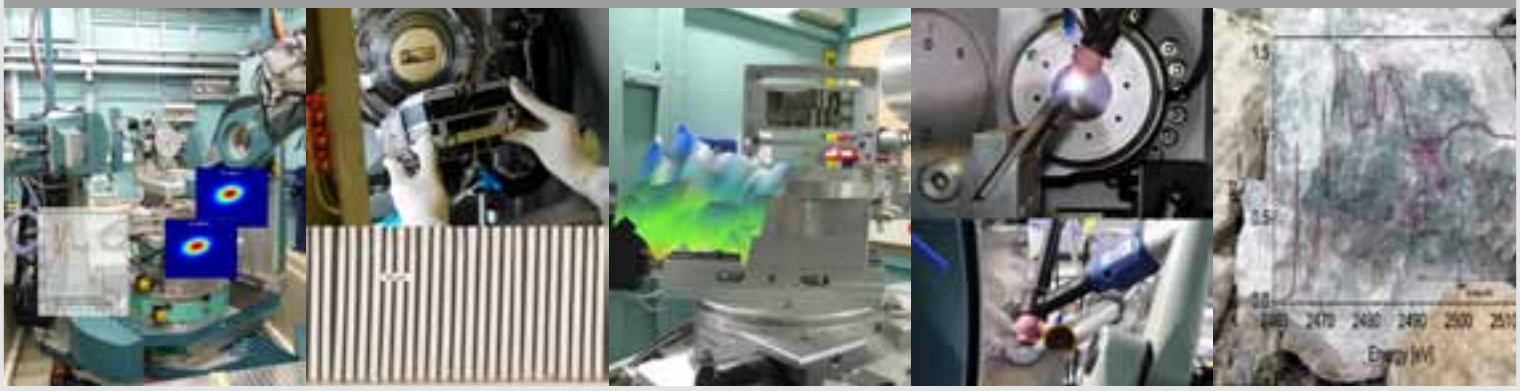

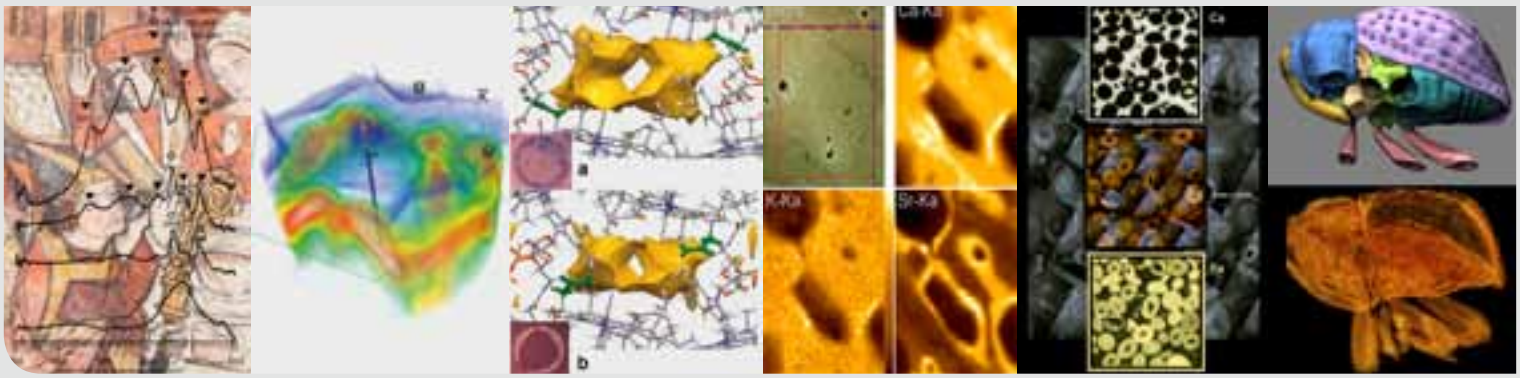

KIT - University of the State of Baden-Wuerttemberg and
National Research Center of the Helmholtz Association

NANO

X-ray diffraction (HR-XRD) with highest angular resolution

Anomalous scattering

Coherent scattering

LIGAI , II, III

Mask fabrication
Thin Microstructures

Deep X-ray lithography

Ultra deep X-ray lithography

XAS

Extended X-ray absorption fine structure (EXAFS)

X-rayabsorption near edge fine structure (XANES)

Q-EXAFS

PDIFF

X-ray powder diffraction (XRPD)

Roentgenography

Single crystal diffraction

SUL-X

X-ray diffraction (XRD)

Fluorescence spectroscopy (XRF)

X-ray absorption spectroscopy in μ-focus

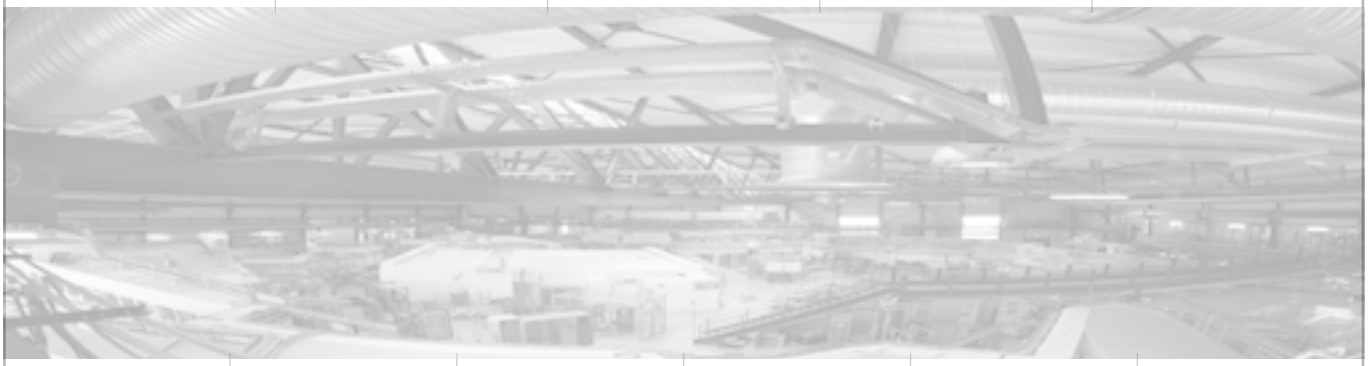

IR 1 / IR 2

Infrared / THz-spectroscopy, -ellipsometry, -microscopy

Infrared / THz Spectroscopy, Ellipsometry, Microscopy and Imaging near field nanospectroscopy

WERA

Soft X-ray spectroscopy, microscopy, and spectromicroscopy:
PES
NEXAFS
SXMCD
Imaging (PEEM)
μ-PES, μ-NEXAFS, μ-SXMCD

SCD

Single crystal diffraction

Single / Multiple anomalous dispersion (SAD/ MAD)

FLUO

X-ray fluorescence analysis (XRF)

X-ray fluorescence microprobe (μ-XRF)

Total X-ray reflection fluorescence (TXRF)

INE

Spectroscopy of actinide samples

TOPO-TOMO

Conventional X-ray topography

2D, 3D absorption-

Phase-contrast imaging

Coverpage:
View of the ANKA-Hall and examples of research results from ANKA's beamlines

Contents

Preface Prof. Dr. Tilo Baumbach

Dear ANKA-associates,

welcome to the ANKA Annual Report which covers the period from mid 2009 to mid 2010.

With this brochure we present you a summary of scientific activities at ANKA throughout the last year. This Annual Report and a new edition of ANKA's Instrumentation Book are delivered on a CD-ROM. The latter exhibits instrumental improvements and extensions due to major upgrades of the beamlines XAS, PDIFF, TOPO-TOMO, the beamlines IR2, UVCD-CD12 as well as the automated LIGA production beamline FELIG3 becoming operational, and the new NANO beamline being in the last stages of its commissioning phase. There are also a presentation of some facts and figures on ANKA's operation and science, and examples of our public and academic-educational activities.

ANKA has completed its south-west hall extension housing the KIT Nanolabs. Civil-engineering activities on the north-west (future IMAGE beamline) and south-east hall extensions (future KNMF labs and a supplementary lab for the CAT-ACT beamline) will commence in spring 2011 and are planned to be finished in autumn 2011.

ANKA has consolidated its role as a national German light source. To successfully continue its ambitious instrumental extension projects, to create maximum possible return of investment in its user operation, and to increase its scientific outreach on an international level by strong in-house research at a given, limited number of personnel resources ANKA's management is advised by newly established Scientific (SAC) and Machine Advisory Committees (MAC). These committees meet twice a year and provide their recommendations in written form. Both committees as well as the Referees of the latest PNI programme evaluation positively recognize ANKA's vision and efforts to integrate synchrotron techniques with large-scale complementary preparation and characterization tools. A key recommendation is *to continue the strategy of ANKA and to take advantage of the full potential in supporting and using ANKA*. In addition, a request to address the problems of understaffing especially of beamline personnel, also in view of strengthening the in-house research capabilities, was issued, and a concept to provide attractive options for former DORIS III users was asked for. ANKA has provided such a concept.

ANKA's proposal for building a new linac-based facility for broadband infrared/THz radiation, TBONE (Terahertz Beam Optics for New Experiments), is pursued in a step-wise fashion: In collaboration with CERN and PSI the test facility FLUTE (*Fern-infrarot Linac- Und Test-Experiment*) with normally conducting 3-GHz-RF cavities will be erected at ANKA to gain experience with the generation of 100-Hz-pulsed, coherent broadband THz radiation. FLUTE is foreseen as a pump source for the Swiss FEL.

We cordially thank our users and colleagues for their high-level research, their fruitful collaboration, and competent exploitation of ANKA's beamlines and of the ensemble of complementary experimental techniques and know-how at KIT.
Based on state-of-the-art experimental infrastructure available at ANKA I do expect a high scientific visibility of ANKA throughout the next year.

Prof. Dr. Tilo Baumbach

Scientific Highlights

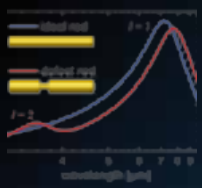

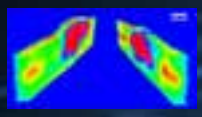

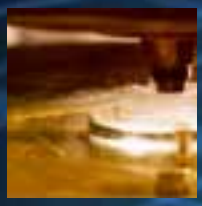

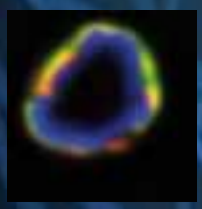

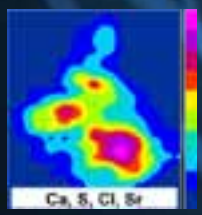

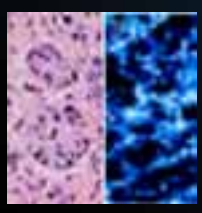

In-situ investigation of polyamide 6 crystallisation in presence of nano-structured impact modifiers

S. Geier[1)], M. Kroh[1)], G. Buth[2)]

1) University of Stuttgart, Institute of Polymer Technology, Pfaffenwaldring 32, 70569 Stuttgart, Germany
2) Karlsruhe Institute of Technology, Institute for Synchrotron Radiation, Hermann-von-Helmholtz-Platz 1, 76344 Eggenstein-Leopoldshafen, Germany

Due to their outstanding mechanical and chemical properties polyamides are used in a wide variety of products, such as textiles, automotives, carpet and sportswear. One of the most important engineering plastics is polyamide 6 (PA 6), because of its high mechanical stiffness as well as high abrasive and medium resistance. The basic building block (monomer unit) of PA 6 is –NH–$(CH_2)_5$–CO–. PA 6 consists of long chains of these monomers, partially being amorphous and partially forming microscopic crystalline structures. For this reason the state of this material is termed "semi-crystalline".

At about 53 °C a glass transition occurs. At room or lower temperatures the chain segments in the amorphous phase are frozen. This leads to rather limited toughness properties of the material under impact loading, a disadvantage for many applications. A common approach to improve the impact behaviour is to add a rubber-like ("elastomeric") second phase. Care has to be taken that the elastomeric phase is regularly dispersed in the PA 6 homopolymer matrix. The elastomeric phase interrupts the fracture propagation and lowers the stress concentration during deformation. This energy absorbing mechanism results in a significant enhancement of the toughness.

In this study PA 6 was blended with a nano-structured PA 6/ Polyether block copolymer (PA 6-copo) as an impact modifier. Preliminary DSC studies have shown a significant change of melting as well as crystallization behaviour of the PA 6-matrix in presence of the impact modifier.

Our aim was to gain microscopic insight into the stucture and crystallization process of PA 6 with and without impact modifier by *in-situ* wide-angle X-ray scattering.

For the *in-situ* X-ray investigations the samples are kept in a closed chamber terminated by two aluminium windows that are nearly transparent for X-rays in a kind of furnace (Linkam hot stage). The temperature of the furnace is controlled by a PC that allows to execute arbitrary temperature profiles. We used it to cool down the samples from the molten state (260° C) at well-defined cooling rates of 10 K/min and 100 K/min while irradiating them with a collimated monochromatic beam of X-rays with a diameter of 0.5 mm.

The X-ray wavelength λ had been set to 0.1 nm. According to the Planck relation

$$E = h \times c / \lambda$$

this corresponds to a photon energy E of 12.4 keV.

The hot stage is mounted in the center of a diffractometer (Bruker AXS D8) equipped with a CCD area detector for X-rays (SMART APEX) (see Figure 1).

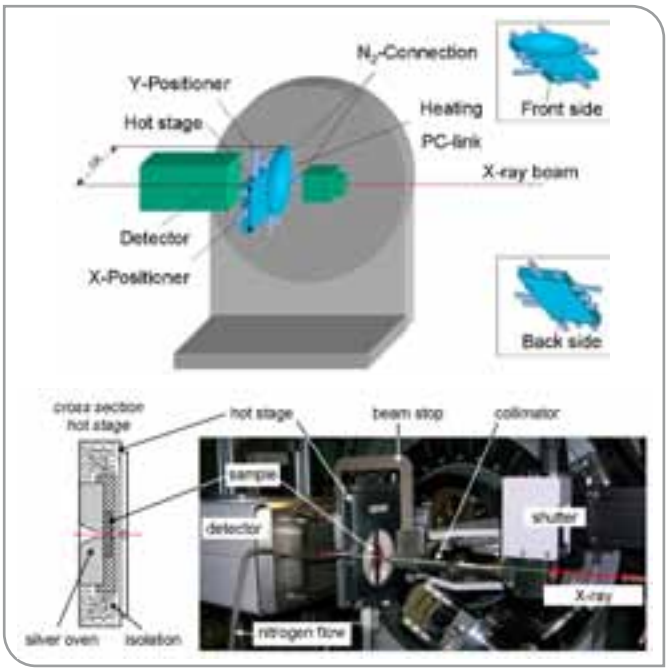

Figure 1:
Schematic of the experimental setup with the Linkam hot stage in the center of the diffractometer.

The CCD detector records the X-rays scattered by fluctuations of the electron density in the sample. Within crystalline domains the electron density fluctuates periodically, allowing for a constructive interference of the scattered X-ray waves in certain spatial directions (see Figure 2) according to the Bragg equation

$$n \times \lambda = 2 \times d_{hkl} \times \sin \theta$$

Here n is the order of diffraction (an integer indicating the number of wavelengths that can be squeezed between two neighbouring lattice planes), d_{hkl} is the distance between two lattice planes in a spatial orientation indexed by a triplet of integers (hkl), and θ is the grazing angle between incident beam and the lattice planes. Thus 2 θ is the angle between incident and scattered beam, repeatedly referenced below.

permit this, we took reference frames from LaB_6, a well established lattice parameter and line profile standard.

We recorded temperature profiles of X-ray scattering spectra from native PA 6 and from PA 6 with different concentrations of an impact modifier (PA 6-copo). Details on the sample preparation and sample geometry can be found in the CD version of the ANKA annual report 2010.

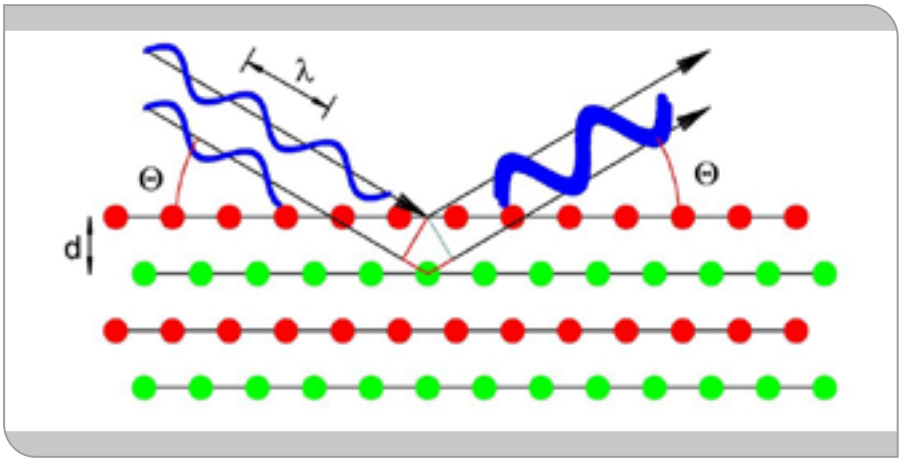

Figure 2:
Principle of diffraction of X-rays from a crystal.

When the path difference of a photon scattered from the lattice plane of a crystal with respect to the neighbouring lattice planes is an integer multiple of the photon wavelength, constructive interference occurs. In the corresponding spatial direction diffracted X-ray intensity can be observed. In the other directions there is no diffracted X-ray intensity because of destructive interference.

Since the crystalline domains are randomly oriented in space, they do not give rise to distinct diffraction spots but to cones of diffracted X-ray intensity, showing up as sharp X-ray illuminated rings on the detector. In contrast the amorphous domains give rise to a spread-out distribution of the scattered intensity with broad maxima resulting from short range order of the atoms making up the polyamide. It is thus possible to determine the degree of crystallinity of a polymer by X-ray scattering. In a temperature dependent *in-situ* experiment the onset of crystallization and the crystal modification can be precisely detected as a function of temperature and temperature slope.

At a given sample temperature all information that can be gained from this experiment is contained in a 1-dimensional I(2θ) X-ray intensity spectrum. Use of an area detector is still essential for this type of experiment, since the exposure time per temperature step is limited by the requirements of the temperature profile, and by radially averaging the intensity along a diffraction ring on the detector the photon counting statistics is dramatically improved. For the same reason use of synchrotron radiation is crucial for this experiment. A prerequisite for the correct radial averaging is a precise knowledge of the detector distance and the beam center coordinates on the detector. To

Depending on cooling conditions PA 6 can develop two different stable crystal modifications, termed "α" and "γ". Moderate cooling usually leads to the formation of the α-modification, revealed by the crystalline reflections $(200)_\alpha$ at 2θ = 13.3° (corresponding lattice plane spacing of d = 0.432 nm) and $(002/202)_\alpha$ at 15.4° (d = 0.373 nm). However, quenching or the interaction with fillers results in formation of the γ-phase, revealed by the intense reflection $(001)_\gamma$ at 13.9° (d = 0.413 nm). (Information on the crystal system and the lattice parameters of both modifications is provided in the CD version of the ANKA annual report.).

For the investigated materials the Table 1 below summarizes the onset of crystallization temperatures (T_{onset}) for the characteristically reflections of the PA 6 α- as well as γ-modification. Using a cooling rate of 10 K/min all blends develop the reflections of the α-modification at almost the same onset temperatures as PA 6. In comparison to the impact modifier itself (PA 6-copo) the onset temperatures of the $(200)_\alpha$ and $(002/202)_\alpha$ reflections decrease by about 15 and 20 K, respectively. This shows that the non-crystallizable polyether phase incorporated within the PA 6 chains of the PA 6-copo reduce the molecular order and mobility which results in a reduction of the crystallization kinetic.

Applying a cooling rate of 100 K/min PA 6 still develops the α-form, however at lower onset temperatures (Figure 3a). Again, the PA 6-copo shows a totally different behaviour. Because of the increase of the cooling rate the predominant modification is the γ-form. The diffraction patterns during cooling in Figure 3b) show the intense $(001)_\gamma$ reflection of the γ-form whereas only the $(200)_\alpha$ reflection of the α-form is well established. For the blends with lower filler contents (up to 16.7 mass-%) still the formation of the α-form is recognizable (Table 1). However, at a content of 16.7 mass-% the influence of the crystallizable impact modifier on the crystallization behaviour of PA 6 is visible.

The T_{onset} for the $(200)_\alpha$ and $(002/202)_\alpha$ reflection decreases by about 15 and 10 K, respectively (Table 1). At a filler content

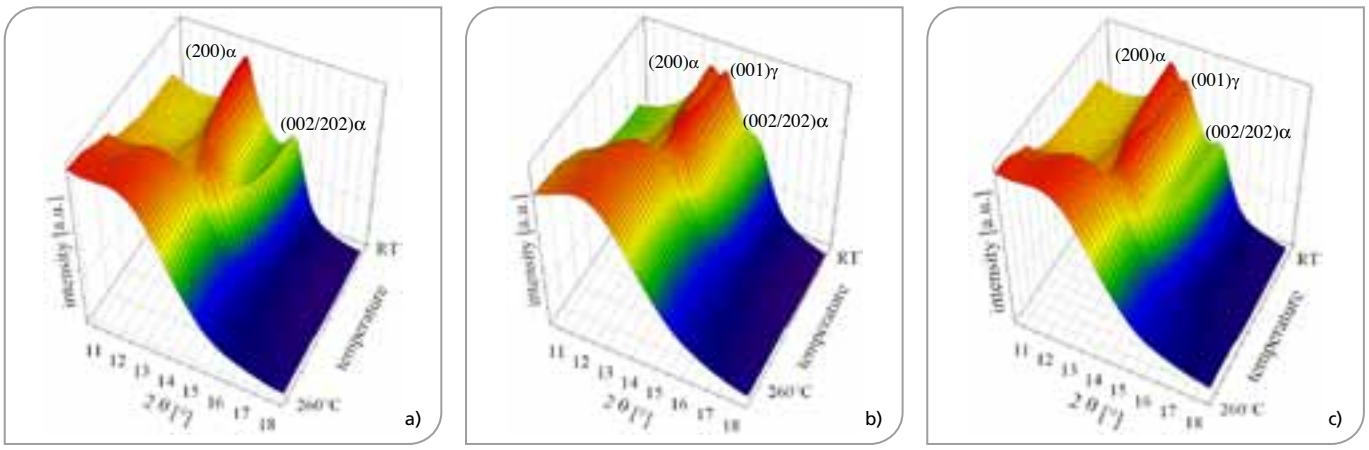

Figure 3:
Diffraction patterns during cooling (100 K/min); a) PA 6, b) PA 6-copo (impact modifier), c) PA 6 + 33.3 mass-% PA 6-copo.

cooling rate	crystalline reflection	PA 6		PA 6-copo		+ 8.3 mass-% PA 6-copo		+ 16.7 mass-% PA 6-copo		+ 33.3 mass-% PA 6-copo	
		T_{onset} [°C]	2 θ [°]	T_{onset} [°C]	2 θ [°]	T_{onset} [°C]	2 θ [°]	T_{onset} [°C]	2 θ [°]	T_{onset} [°C]	2 θ [°]
10 K/min	$(200)_\alpha$	185	13.6	170	13.5	186	13.6	187	13.6	186	13.6
	$(002/202)_\alpha$	146	14.4	122	14.5	146	14.4	146	14.4	145	14.4
100 K/min	$(200)_\alpha$	152	13.6	62	13.2	153	13.6	138	13.6	66	13.1
	$(002/202)_\alpha$	89	14.4	-	-	90	14.5	80	14.6	59	14.8
	$(001)_\gamma$	-	-	125	13.5	-	-	-	-	145	13.5

Table 1:
Onset temperatures (T_{onset}) of the crystalline reflections at different cooling rates.

of 33.3 mass-% the blend shows again the formation of both crystal modifications (Figure 3c). Compared to the PA 6-copo the α-form is more intense established than the γ-form. Consequently, by the strong interaction between PA 6-copo as a crystallizable impact modifier in PA 6 the chain mobility of the matrix is affected. This results in both, the transition of α- to γ-modification as well as a decrease of the crystallization kinetic of PA 6. Based on the arrangement of the polymer chains the γ-form has a lower density which leads to a decrease in mechanical stiffness and an increase in ductility. Therefore the knowledge of structure formation of the PA 6-matrix in present of the impact modifier allows a further adjustment of the balance between stiffness and toughness properties of the blend.

This work has been subsidized by the German Research Foundation (DFG) in the project GO 579/11-1 and the project SCHM 746/74-1.

Detection of symmetry forbidden antenna resonances in individual metallic nanorods

D. Weber[1)], F. Neubrech[1)], A. Garcia-Etxarri[2)], J. Bochterle[1)], H. Shen[3)], M. Lamy de la Chapelle[4)], G. W. Bryant[5)], J. Aizpurua[2)], and A. Pucci[1)]

1) Kirchhoff-Institut für Physik, University of Heidelberg, 69120 Heidelberg, Germany
2) Centro de Física de Materiales CSIC-UPV/EHU and Donostia International Physics Center DIPC, 20018 Donostia, Spain
3) Institut Charles Delaunay, FRE CNRS 2848, Université de technology de Troyes, 10010 Troyes cedex, France
4) Laboratoire CSPBAT - FRE 3043, UFR SMBH, Université Paris 13, 93017 Bobigny, France
5) National Institute of Standards and Technology, Gaithersburg 20899 MD, USA

Metal nanoparticles offer a huge variety of applications in today's technologies (e.g. bio-sensing) because their optical excitations (so-called localized surface plasmon resonances) can be tuned over a broad frequency range from THz radiation to visible light. In analogy to radio frequency antennas, where electron oscillations can be excited resonantly by light if one half of the wavelength λ of the light equals the length *L* of the antenna ($L = \lambda/2$), metallic nanorods (nanoantennas) with lengths in the µm-range show such resonances in the THz to infrared (IR) spectral range.

Of special interest is the huge electromagnetic near-field enhancement at the tip ends in case of resonance, because it can be exploited for highly sensitive detection of adsorbed molecules. In other words, the nanoantenna acts as an amplifier of light intensity, therefore making detection of small amounts of molecules possible (below one attomol for IR spectroscopy, single molecules for Raman spectroscopy in the visible range).

The resonant wavelength λ_{res} of the antenna does not only depend on the length *L* but also on the kind of metal, the diameter *D*, the overall shape of the antenna and on the substrate polarizability. Nevertheless, the ideal $L = \lambda/2$ antenna behavior can serve as qualitative model for principle understanding of symmetry effects of high aspect-ratio particles ($L >> D$). Including higher harmonics, resonances occur according to the relation

$$L = l\ (\lambda_{res}/2), \qquad l = 1, 2, 3, \ldots. \qquad (1)$$

where the integer *l* denotes the order of the resonance.

Figure 1 schematically shows the standing waves of free electron oscillations with their corresponding charge carrier concentrations (positive charges originate from a lack of electrons) at a fixed time. On the right hand side of Figure 1, the overall electric dipole moment *p* of each mode is indicated. Since the partial dipole moments in even order modes cancel each other, these modes cannot be excited by light at normal incidence and are therefore referred to as "dark modes". In contrast to bright

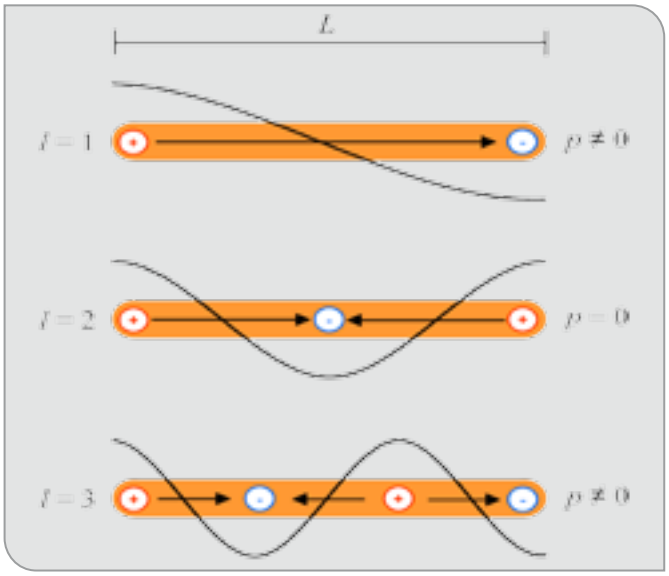

Figure 1:
Schematic representation of the first three resonance modes of an antenna with length *L*. The order *l* is indicated on the left. The electrons are oscillating and form standing waves, the charge carrier concentrations of which are shown at a fixed time. Due to the separation of charges, dipole moments are formed and indicated by arrows. Since the overall dipole moment *p* of even order modes vanishes, they cannot be excited by normal incident light.

modes (odd *l*), such dark modes of a perfect-shaped nanorod should not appear. However, as we experimentally detected and theoretically explained dark modes become optically active if the inversion symmetry of the rod is disturbed, even for smallest disturbances.

The effect of symmetry breaking from a small defect was shown for gold nanorods with quadratic cross-sections (100 x 100 nm²) and lengths between 1 and 2 µm (width and height of about 100 nm) that were produced by electron beam lithography (EBL) on planar zinc sulfide (ZnS) substrates with very low surface roughness. However, any scratches in the substrate surface can lead to modifications of the nanorod's shape, which is a production error that cannot be avoided completely.

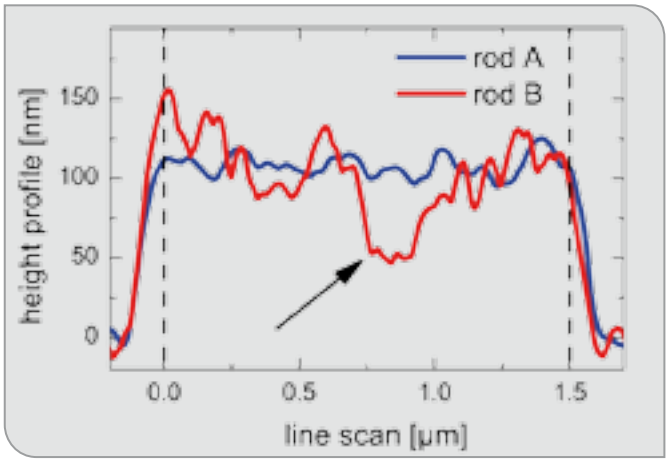

Figure 2:
Atomic force microscopy line scans along two similar nanorods (L = 1.5 µm). While rod A (blue curve) features a rather smooth height profile, the symmetry of rod B (red curve) is distorted by a "valley" which is indicated by an arrow.

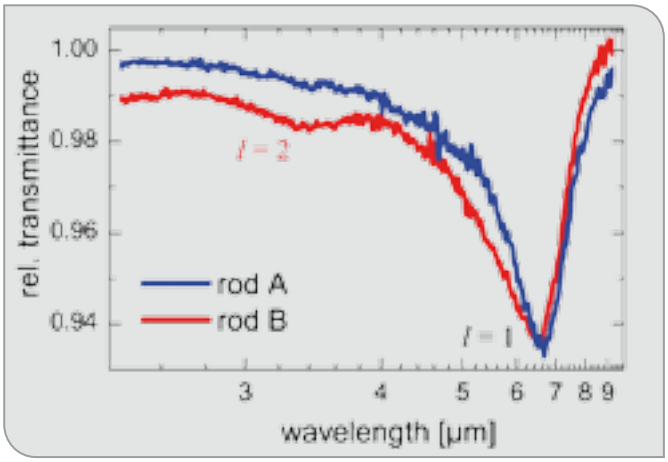

Figure 3:
Relative IR transmittance spectrum of the individual rod A (blue curve, ideal nanorod) and the individual rod B (red curve, defect nanorod). The height profiles are shown Figure 2 and the resonance order l is indicated. The even order mode l = 2 at around 3.5 µm only appears for the "defect" rod B.

In Figure 2, atomic force microscopy (AFM) line scans of two different nanorods (L = 1.5 µm) along their long axis are shown. Obviously, the height profiles of the two nanorods differ in surface roughness: whereas nanorod A features a more or less smooth surface, nanorod B exhibits several large steps and a "valley", which is indicated by the arrow. Since this groove is not located in the center of the nanorod, inversion symmetry is clearly broken. According to equation (1), we expect such resonance excitations of micrometer-sized nanorods in the IR spectral range. Therefore, we use IR spectroscopy to investigate the optical behavior of nanorods. With IR light, the effect of symmetry breaking can be spectroscopically detected, which is faster and more convenient than scanning the atomic force along the nanorods. Since a high intensity light source is beneficial for the clear proof of the spectral changes due to defect-related symmetry breaking, we used the synchrotron light source ANKA to demonstrate the effect for individual nanorods. Perfect nanorods absorb and scatter light at the wavelength λ_{res} only for odd orders l. The two spectra of single nanorods (as relative transmittance spectrum, normalized to a spectrum of the bare substrate) shown in Figure 3 belong to the two nanorods A and B from Figure 2. Since they both have nearly the same length L, they feature nearly the same fundamental resonance (indicated by l = 1) at around 7 µm. The even order l = 2 at around 3.5 µm is only excited in rod B with structural defects (see Figure 2).

The more perfectly shaped rod A does not exhibit this dark mode. Theoretical simulations also fully support the experimental findings. Figure 4 shows calculated far-field intensities for a perfect cylindrical rod (blue curve) and a "defect" rod with a

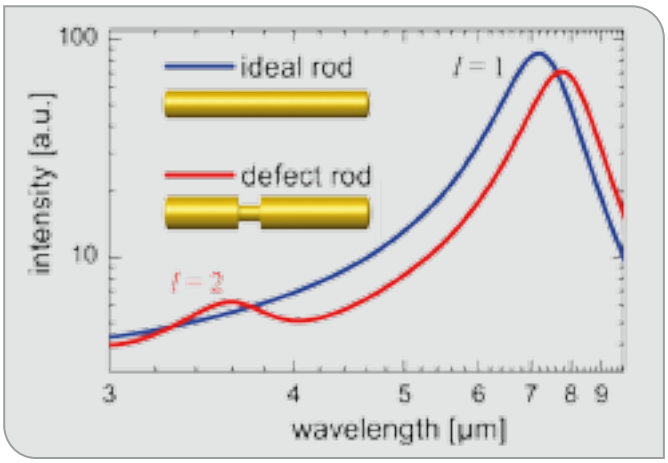

Figure 4:
Simulated scattering intensity (logarithmic scale) of an ideal (blue line) and an inhomogeneous (red line) nanorod with L = 1.5 µm. The detailed shapes of the nanorods are sketched and the order l of the resonances is indicated. Due to the structural defect, the second order appears in the spectrum.

neck, offset from the rod center (red curve). In fact, the second order mode at around 3.5 µm really originates from the defect shape of the nanorod.

In conclusion, dark modes in normal IR transmittance spectra of individual gold nanorods appear if defects have broken inversion symmetry. Such defects may be induced by substrate surface scratches, for instance or imperfections arising from the preparation of the nanorods. Therefore, the spectroscopic observation of even order modes could be used as an indicator for possible imperfections in nanorod structure and thus be applied for production process control.

3-Dimensional X-Ray Diffraction Imaging Study of Damage to Silicon Wafers

D. Allen[1)], J. Stopford[1)], J. Wittge[2)], M.C. Fossati[3)], J. Garagorri[4)], E. Gorostegui-Colinas [4)], P.J. McNally[1)], T. dos Santos Rolo[5)], P. Vagovic[5)], M.M. Morshed[1)], O. Aldrian[1)], A.N. Danilewsky[2)], M.R. Elizalde[4)], D.K. Bowen[3)], and B.K. Tanner[3)]

1) Dublin City University, The RINCE Institute, Dublin, Ireland
2) Universität Freiburg, Kristallographie, Instut für Geowissenschaften, Freiburg, Germany
3) Durham University, Department of Physics, South Road, Durham, DH1 3LE, United Kingdom
4) CEIT and Tecnun (University of Navarra), San Sebastian, Spain
5) Karlsruhe Institute of Technology, Institute for Synchrotron Radiation, Hermann-von-Helmholtz-Platz 1, 76344 Eggenstein-Leopoldshafen, Germany

We describe the use of 3-dimensional X-ray diffraction imaging, (3D-XRDI) in conjunction with image processing algorithms to characterise silicon damage sites, and examine the physical processes which have occurred as a result of the damage. Section Transmission (ST) topographs were taken at the TOPO-TOMO beamline of the synchrotron ANKA. 3D-XRDI was realised by stacking of section X-ray transmission topographs of the damaged regions using open source tomographic algorithms (ImageJ). ImageJ plugins were used for automated image alignment and image processing.

Damage to silicon (Si) wafers can occur in a number of ways. It is known that wafer handling introduces micro-cracks at the wafer edge. While most of this damage appears to be harmless during production, there exists the possibility that, particularly with Rapid Thermal Annealing, these micro cracks can produce larger, long range cracks that can cause the wafer to fail catastrophically. Wafers can be subjected to process induced damage (e.g. plasma arcing) and it is shown here that even the laser marking process can introduce strain into the Si wafer.

This study used both 20 x 20 mm (100) Si wafer pieces and whole 200 mm (100) Si wafers. Nano indents with forces ranging from 2 N to 10 N using a Vickers (diamond tip) and 100 mN to 600 mN using a Berkovich (pyramidal tip) were introduced to both the wafers and the wafer pieces as a means of introducing controlled strain. The samples were then annealed for 60 seconds at 1000°C with a 60 second ramp up and 60 second cool down. A second set of samples were subjected to plasma arc damage to simulate common process induced damage. This plasma arc damage samples were generated in a plasma chamber filled with Argon (Ar) gas at 3 mbar pressure. The chamber design was that of a parallel plate with the wafer as the grounded electrode. The current drawn by the arc was ~200 mA at the damage site.

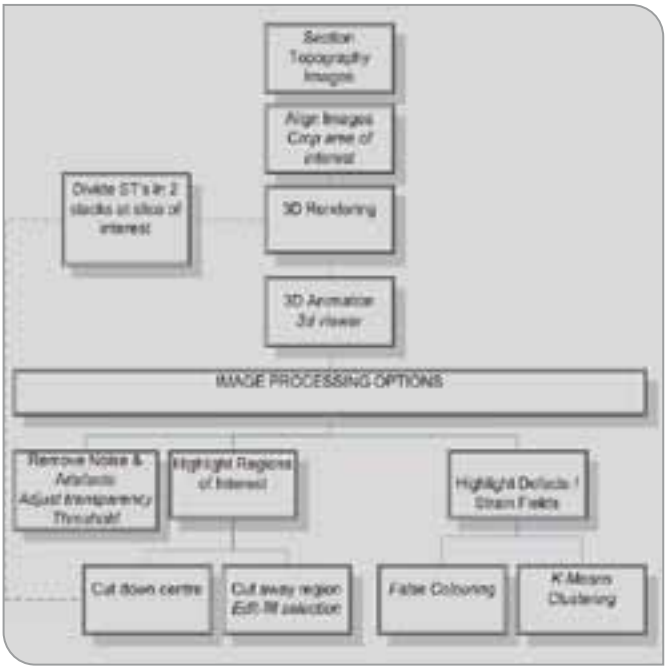

Figure 1:
Basic 3D rendering and image processing steps.

The ST topographs were recorded using a PCO.4000 14 bit cooled CCD camera system using 3.6x magnification optics to give an effective pixel size of 2.5 x 2.5 µm with the incident beam collimated to 10 mm x 15 µm in size by a final vacuum slit system positioned 30 cm from the sample. The samples were mounted on a high precision XY translation stage, tilted to 12° and the camera positioned to capture the *022* reflection of the (100) Si samples.

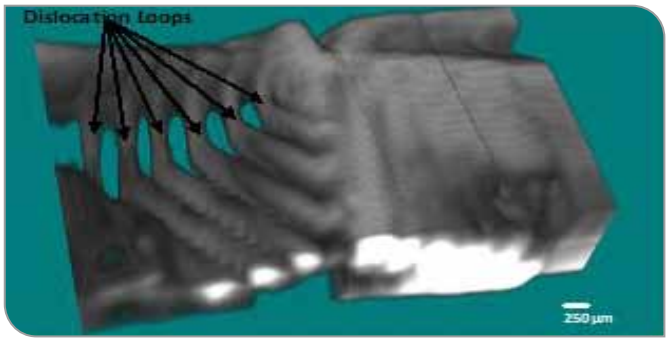

Figure 2:
3D-XRDI image of dislocation half loops.

Figure 3:
3D-XRDI image of a wafer laser mark. The red arrow points to the strain fields created by the laser mark process.

The sample was them stepped through the beam in 15 µm steps with the acquisition time optimised to 0.5 second per picture, thus obtaining a series of 'slices' across the damage sites. The ST topographs were then rendered into 3D images using the *ImageJ* software suite. Figure 1 shows the image acquisition and processing steps.

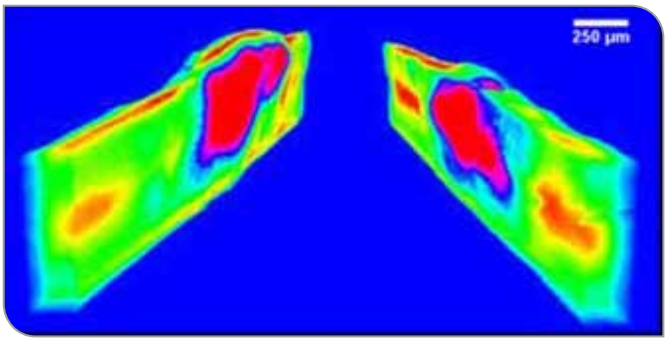

Figure 4:
3D-XRDI of plasma arc damage. The image has been 'cut' down the centre and false colouring applied. The red region corresponds to the area with the highest strain levels.

Figure 2 shows the propagation of dislocation half loops from a thermally annealed sample running from the top surface to the back side of the wafer. The half loops glide at an angle of ~54° to the surface corresponding with the {111} series of glide planes. Figure 3 shows a 3D-XRDI rendering of a laser mark on a 200 mm wafer. This shows the strain field, highlighted by the arrow, emanating from the laser marks and propagating through the wafer.

Figure 4 shows the use of K-means clustering and false colour imaging to highlight a region of interest i.e. that of plasma arc damage on a Si sample. The red region corresponds to the area of highest strain and shows that the strain field propagates out from the damage site in all directions, penetrating up to 2/3 of the way through the bulk Si.

This investigation demonstrates that damage caused by wafer handling, shipping and processing does have an effect on the integrity of the wafer structure and that 3D-XRDI has extensive capabilities for future non-destructive characterisation of this type of wafer damage.

Local Structure and valence state in Am containing MOX fuel

M. Vespa[1)], R. Jovani-Abril[1)], M. Rini[1)]

1) European Commission, Joint Research Centre, Institute for Transuranium Elements, Postfach 2340, D–76125 Karlsruhe, Germany

The Generation IV (Gen IV) initiative foresees sustainable and safe use of nuclear energy for future generations. Three of the systems selected operate with fast neutron spectra, with the novelty that they will transmute their own actinide waste, thereby dramatically reducing the long term radiotoxicity of the spent fuel. Furthermore, proliferation resistance will be enhanced by grouped actinide separation and conversion into new fuel. Thus, the new advanced fuels will contain U, Pu and the minor actinides (MA = Np, Am, Cm). The minor actinides can be deployed in all the $(U,Pu)O_2$ fissile fuel (homogeneous reactor recycling) or in dedicated targets, e.g. $(U,MA)O_2$ (heterogeneous reactor recycling).

An important fuel parameter in the fuel specification is the oxygen/metal (O/M) ratio. This is particularly important for Am, as at high temperatures oxygen loss, i.e. Am reduction, would result in deleterious cladding corrosion. Therefore low O/M ratios, close to O/Am = 1.5 are preferred. In contrast, however, lower O/Am ratios can result in lower thermal conductivity of the fuel, and concomitant higher risk of melting, so that the operating power (i.e. MA content) may be curtailed.

In the present study $(U,Am)O_{2-x}$ has been synthesised with 10 and 20% Am, and the local structure and valence state of U and Am has been investigated by X-ray absorption spectroscopy fine structure (XAFS) and near-edge structure (XANES) at the INE Beamline at the ANKA. The combination of XAFS and XANES techniques provides atomic level information on the actinide mixed oxides. Direct information on the valence state, nearest and next nearest neighbour distances, coordination number and system disorder are obtained.

Pellets of $(U,Am)O_{2-x}$ were prepared in the Minor actinide laboratory (MALAB) at the Institute for Transuranium Elements (ITU) by a sol-gel method coupled with an infiltration process. The sol-gel step is, in fact, a gel supported precipitation during which the U nitrate solution is conditioned by organic polymers and transformed, by a rotating cup, into droplets, which are collected in an ammonia bath. The resulting microspheres or beads of UO_2 are washed, dried and calcined, after which they are infiltrated by an Am nitrate solution and dried at room temperature. After a further calcination step at 800°C, the resulting powder was compacted and sintered at 1650°C under Ar/5%H_2. The product with Am/(U+Am) = 0.088 is composed of a single phase, as determined by X-ray diffraction.

Figure 1:
UO_2 droplets forming during sol-gel process

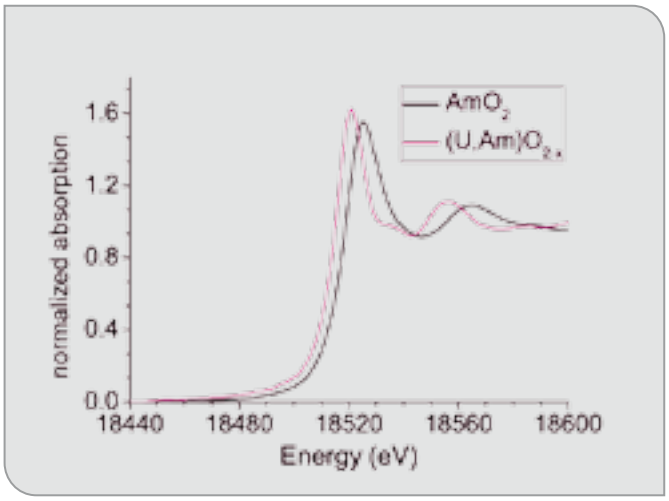

Figure 2:
Normalized absorption spectra of the AmO_2 reference and the $(U,Am)O_{2-x}$ at the Am L_{III} edge

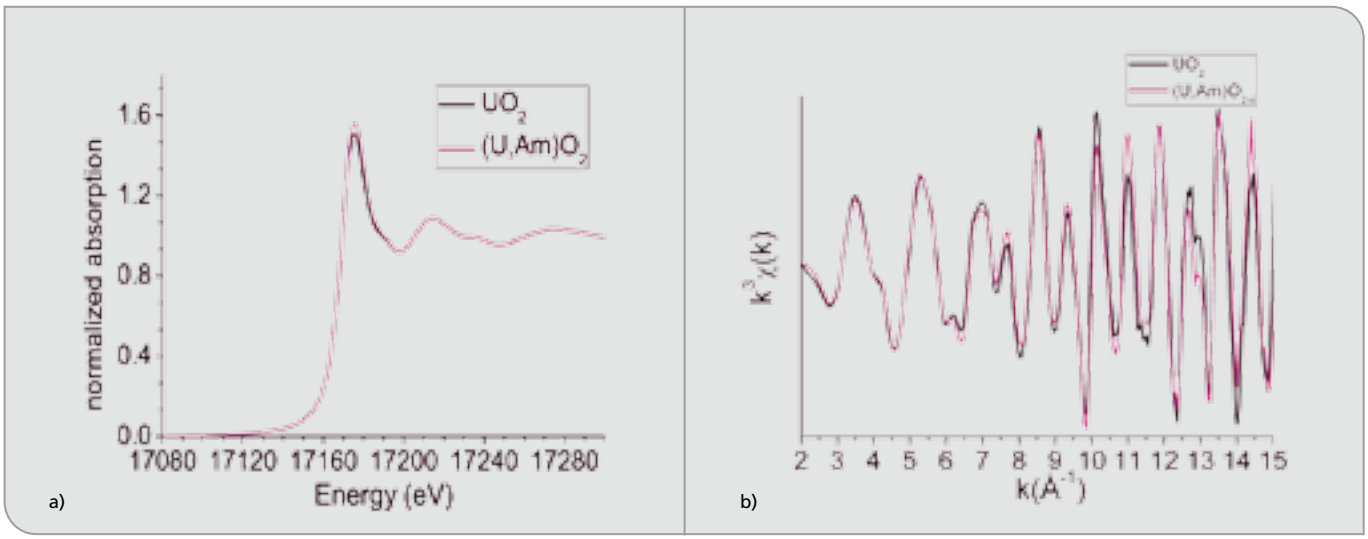

Figure 3:
a) Normalized absorption and b) k^3-weighted XAFS spectra of the UO_2 and $(U,Am)O_{2-x}$ at the U L_{III} edge.

Figure 2 shows the normalized XANES data at the Am LIII edge for the reference AmO_2, and $(U,Am)O_{2-x}$ sample. The edge position of the mixed oxide is shifted to lower energies with respect to the AmO_2 indicating the presence of Am(III). Data analysis show that the AmO_2 has an Am-O distance of 2.30 Å typical for Am(IV), whereas $(U,Am)O_{2-x}$ sample has a much longer distance of 2.43 Å.

At the U_{LIII}, the absorption edge is at the same energy for all samples, and the XAFS oscillations are similar to the UO_2 (U(IV)) (see Figure 3), indicating that the 8.8% Am concentration does not significantly alter the local environment of the U in the $(U,Am)O_{2-x}$ mixed oxide.

The information gained in this study permits a greater understanding of the local structure, than is possible using classical diffraction methods. Further data refinement is underway, and measurements on samples with a higher Am content are being prepared. Ultimately these data will permit qualification of parallel ab initio calculations of the structure of these compounds and will thus make a significant contribution towards the development of multiscale modelling and understanding of GEN(IV) fuels and ultimately their in pile performance.

The nature of thorium in Greek aluminium ores and their residues

A. Godelitsas[1)], P. Gamaletsos[1)], T.J. Mertzimekis[2)], J. Göttlicher[3)] and Ralph Steininger[3)]

1) University of Athens, 15784, Zographou, Greece
2) Institute of Nuclear Physics, NCSR "Demokritos", 15310, Aghia Paraskevi, Greece
3) Karlsruhe Institute of Technology, Institute for Synchrotron Radiation, Hermann-von-Helmholtz-Platz 1, 76344 Eggenstein-Leopoldshafen, Germany

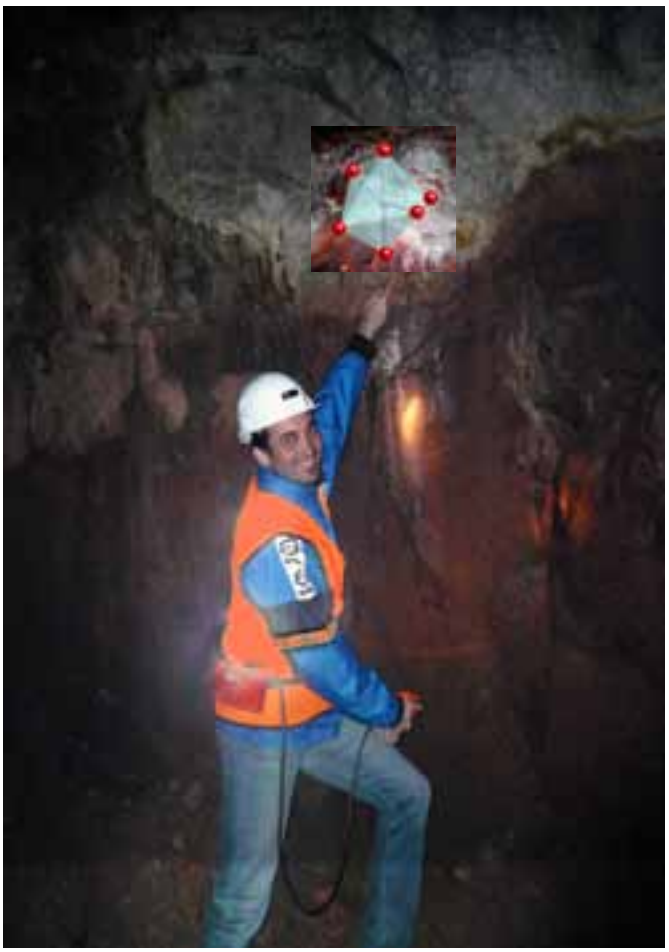

Figure 1:
Underground occurrence of typical Fe-enriched (red-brown) industrial bauxite overlaid with a body of Fe-depleted (white-grey) diasporic bauxite, in an active mine of the Parnassos-Ghiona area, central Greece.

Bauxite was firstly recognized as aluminium (Al) ore in the Les Baux village (southern France) by the French geologist P. Berthier in 1821. This geological material was formed under hot and humid climate in upper Mesozoic Era, more than 100 million years ago, due to intense weathering of various rock types of the ancient continent. After prolonged dissolution of the rocks and subsequent complex geochemical reactions, the insoluble chemical compounds (mostly Al-oxyhydroxides) and residual minerals were deposited into cavities of older limestones (karstic surfaces).

Further geological processes contributed to the final formation of the so-called "karst-type", allochthonous bauxite (ca. 15% of the world deposits), which is predominant in the Mediterranean belt, in contrast to lateritic autochthonus bauxite occurring in Australia, Brazil, India, etc (ca. 85%). Almost one century later, karst-type bauxite deposits, similar to French ones, were exploited in central Greece, in the area of legendary Parnassos Mountain near the Oracle of Delphi. As mentioned by Georgalas 1946 in the journal „*Nature*", the existence of bauxite in Parnassos (and Ghiona Mt.) was announced around 1922, giving possibilities of developing an aluminium industry in Greece.

Nowadays, Greece is the 11th largest bauxite producer in the world (2.22×10^6 tons in 2008). The exploitation of Parnassos-Ghiona deposits, hosted into Mesozoic limestones derived from the Tethys palaeo-ocean, is currently performed by three Greek mining companies (Aluminium of Greece S.A., S&B Industrial Minerals S.A. and ELMIN Hellenic Mining Enterprises S.A.), whereas there is also an Al industrial plant in the Gulf of Corinth. It is now established that the Greek mining industry controls the most significant bauxite reserves in the European Union and Greece is the 17th country in the world regarding alumina production.

Bauxite in general, due to its genesis through surficial and supergene ore-forming processes, acts as a sink of an exceptional number of chemical elements from the whole spectrum of the periodic table. On the other hand, its mineralogical composition, based on major Al, iron (Fe), and titanium (Ti), is rather simple, implying that various elements are present as impurities into Al-oxyhydroxides as well as Fe- and Ti-oxides. The mineralogy of Greek industrial bauxites is also not particularly variable; diaspore and/or boehmite (AlOOH polymorphs), hematite (Fe_2O_3) and

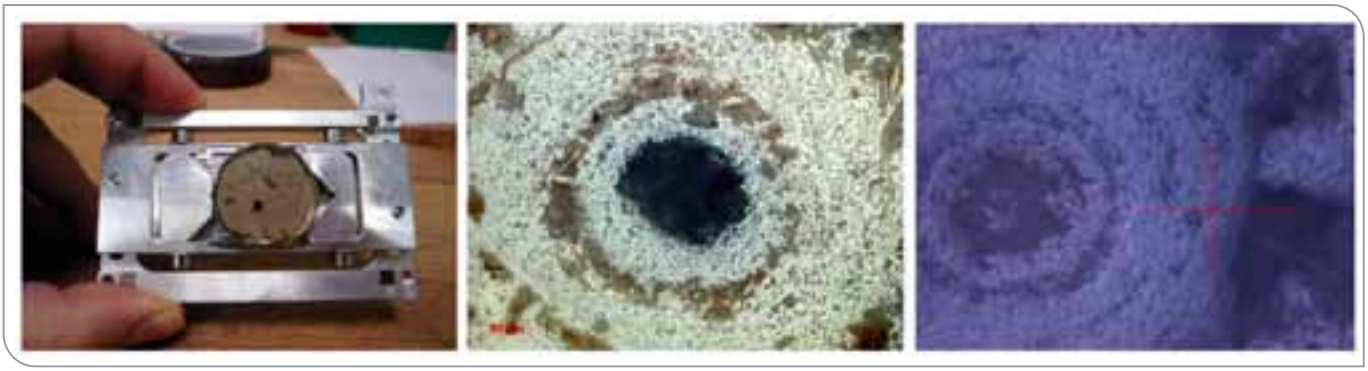

Figure 2:
Fe-depleted diasporic Greek industrial bauxite sample investigated in the SUL-X beamline of ANKA

anatase (TiO_2 polymorph) are the major phases. Typical Fe-enriched (red-brown) bauxite contains 57% Al_2O_3. Of special interest is the high-quality Fe-depleted or "bleached" (white-grey) diasporic bauxite (Figure 1) composed only of diaspore (in some cases Fe-Cr-diaspore) and TiO_2 polymorphs, containing 80% Al_2O_3. The chemical composition of all types of bauxite is, again, complicated and almost all natural elements are present in various concentrations.

According to preliminary results, Greek industrial bauxites, though they are "depleted" in geochemically incompatible elements like Cs, Rb, Ba, K and Sr (Large Ion Lithophilic Elements/LILE), they are highly enriched in geochemically compatible elements such as Cr and V as well as in rare high-field strength lithophilic elements (HFSE) such as Zr, Hf, Nb, Ta, W and Ce. Moreover, they contain significantly increased concentrations of actinides (U and Th), compared to surrounding sedimentry rocks, which are considered to be both penalty elements in the metallurgy and radiotoxic for the environment.

As a result bauxites and their corresponding metallurgical tailings (residues remaining after alumina production using Bayer process) are slightly radioactive.

It should be noted that alumina (Al_2O_3) contains no actinides and therefore all U and Th are practically transferred from the bauxite ore to the residues (the so called "red mud") in the industry. The highest Th concentration corresponds to specific Fe-depleted, white-grey, samples (up to 63 ppm in bulk).

Gamma-ray spectra (HPGe detector) revealed for Fe-depleted bauxite an average of 220 Bq/Kg corresponding to ^{228}Ac (^{232}Th-series), compared to 180 Bq/Kg for typical Fe-enriched bauxite. Evaluation of preliminary bulk geochemical data indicated that Th is correlated to LREE and U, particularly in Fe-depleted bauxite. Moreover, Th is rather correlated to Fe in Fe-enriched bauxite, while there is no evident bulk correlation to Ti for all bauxite samples. The presence of Th in Greek bauxites is known since early '60s from studies of the Rice University (TX, USA) and later papers from the Greek geological survey (IGME) and the "DEMOKRITOS" research institute. However, the above works contain only bulk measurements with regard to the concentration of Th in selected bauxite samples. Additionally, in a series of substantial papers from University of Montpellier (France) and University of Hamburg (Germany), about the geology, mineralogy and geochemistry of Parnassos-Ghiona bauxites, there is no particular information on the distribution and partitioning of Th in the materials.

The aim of the present project was to investigate the solid-state chemistry of Th in Greek bauxites and their residues (red mud remaining after Bayer process and containing 108 ppm Th) by means of synchrotron micro-XRF (X-ray Fluorescence) and –XAFS (X-ray Absorption Fine Structure) spectroscopy at the ANKA SUL-X beamline. It should be emphasized that such Synchrotron-based techniques have never been applied for the study of bauxites before, neither from Greece or another part of the world.

The white-grey bauxite was studied in the form of proper rock slides embedded in epoxy resin (Figure 2) whereas the red mud was also investigated in the form of powder. Thorium compounds (ThO_2, $Th(NO_3)_4$) and pure mineral powders, containing Th in various ppm levels, such as zircon ($ZrSiO_4$), fluoroapatite ($Ca_5(PO_4)_3F$), bastnäsite ($CeCO_3F$) and parisite ($CaCe_2(CO_3)_3F_2$) were used as reference materials.

The Synchrotron spectroscopic investigation of Fe-depleted Greek industrial bauxite proved the presence of Th and revealed that the actinide element is

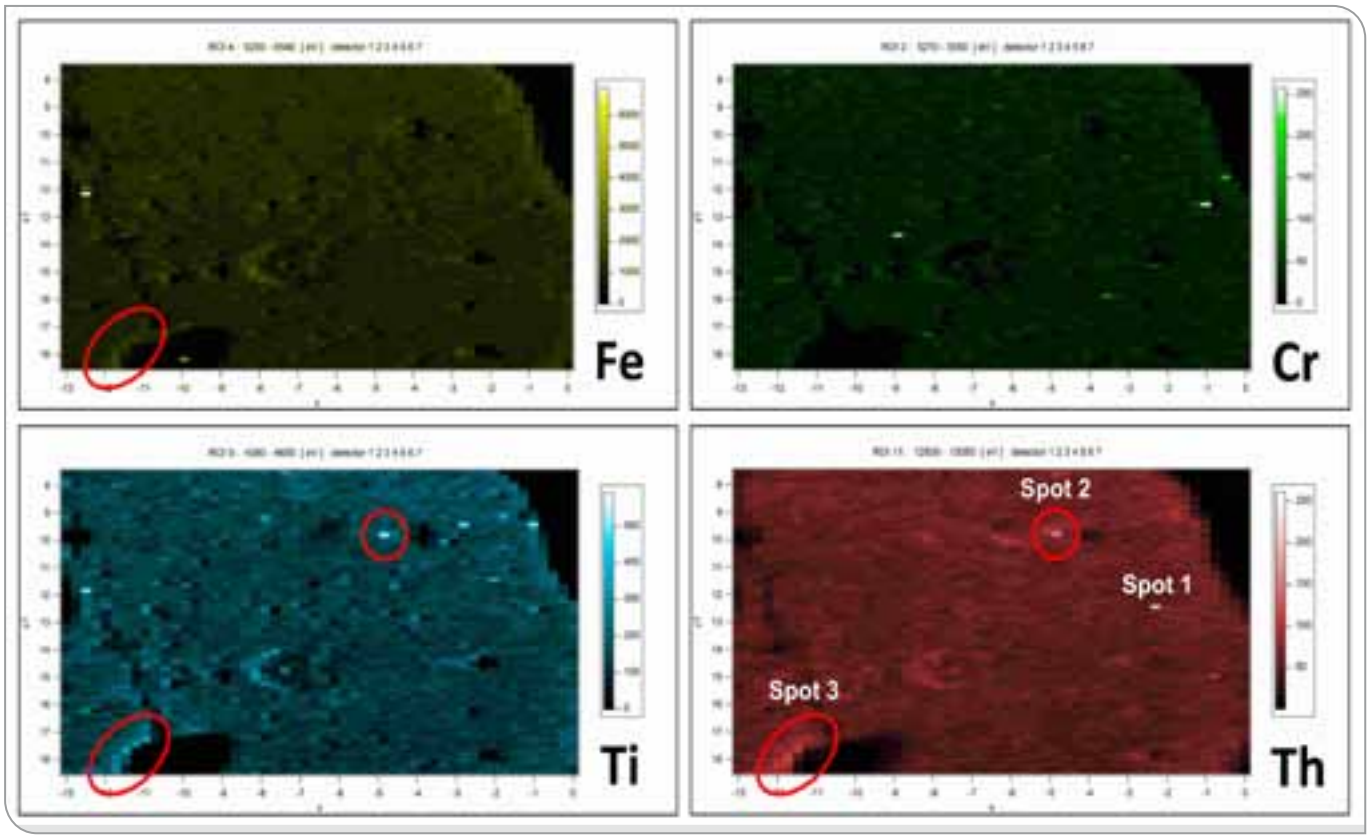

Figure 3:
Synchrotron micro-XRF elemental maps of bauxite and micro-XAFS spectra from Spot 3, the residues (red mud / RM), and reference materials

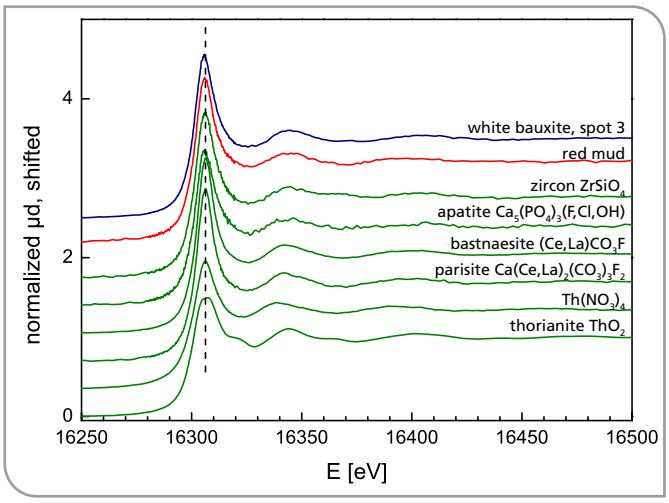

particularly associated with Fe/Ti- and Ti-containing phases into distinct pisoliths.The whiteline positions of the XANES spectra are consistent with the whitelines of Th(IV) reference compounds (Figure 3).

The association of Th with Ti in bauxites is demonstrated for the first time. This can be explained on the basis of the same +4 oxidation state of Th and Ti, despite the relatively large difference in the ionic radius of 6-coordinated Th^{4+} and Ti^{4+} to O-atoms (0.940 Å and 0.605 Å respectively). Relevant works have already indicated the presence of Th in ilmenite ($FeTiO_3$) and rutile occurring in sand deposits. However, in this case, Th is contained in the crystal structure of anatase (a modification of TiO_2), built up by distorted TiO_6-octahedra, which is grown during diagenesis of bauxitic materials. This novel conclusion was complementary supported by advanced laser-based techniques (LA-ICPMS) which revealed an average of 73 ppm Th in anatase grains together with abundant Nb (3356 ppm), Ta (247 ppm) and U (33 ppm).

Further evaluation of the recorded X-ray absorption spectra may also give new insights into the mineralogy and geochemistry of Th in karst-type bauxites, related to the low-temperature partitioning of the actinide element in anatase-type phases.

3D speciation of improved catalysts for H_2 production

W. De Nolf[1)], P. Benito[2)], M. Monti[3)], K. Janssens[1)], S. Bugani[2)], A. Vaccari[2)], F. Basile[2)], G. Fornasari[2)], L. Morselli[2)], E. Scavetta[3)], D. Tonelli[3)]

1) University of Antwerp, Department of Chemistry, Universiteitsplein 1, B-2610 Antwerpen, Belgium
2) Università di Bologna, Dip. Chimica Industriale e dei Materiali, V.le Risorgimento 4, I-40136 Bologna, Italy
3) Università di Bologna, Dip. Chimica Fisica e Inorganica, V.le Risorgimento 4, I-40136 Bologna, Italy

Investigating the inner structure of objects with X-rays, without the need for cutting them, is a common practice nowadays. Few laboratories however, including synchrotrons, can couple this with the extraction of information regarding chemical elements, their state and surrounding. A tomographic technique that combines X-ray Fluorescence and X-ray Powder Diffraction at a synchrotron light source can achieve this with micron resolution for crystalline material.

The production of H_2 from natural gas, a major source for making hydrogen, can in general be achieved via steam reforming (SR) or catalytic partial oxidation (CPO). SR is an endothermic reaction, performed at high temperature (900-1000°C) in the presence of nickel- or rhodium-based catalysts. The thermal conductivity of the catalyst should be high to avoid thermal gradients and allow efficient heat transfer through the whole catalytic bed. CPO on the other hand, is a mildly exothermic reaction that is performed at short contact times. Therefore hot spots and pressure drops must be avoided. Catalysts applied on highly porous metal-foams potentially meet the requirements for SR and CPO, provided that a stable layer of catalyst can be deposited on the foam walls.

The use of electrochemical deposition (ECD) of the active phase on a metal-foam is being investigated to overcome some disadvantages of the traditional

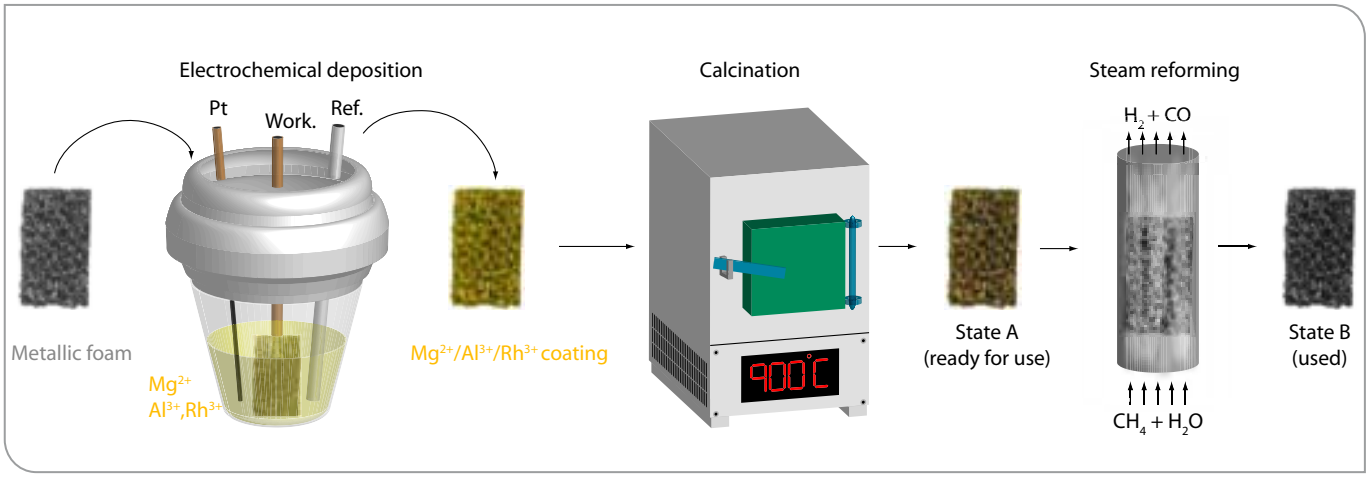

Figure 1:
Schematic representation of the preparation and use of Rhodium-based structured catalysts for hydrogen production from natural gas.

wash-coating procedure such as inefficient coating and pore blockage.

A schematic representation of the preparation and usage of a Rhodium-based structured catalyst is given in Figure 1.

From a solution of nitrates [$Mg^{2+}(NO_3)_2 \cdot nH_2O$] and [$Al^{3+}/Rh^{3+}(NO_3)_3 \cdot nH_2O$] it is possible to form a hydrotalcite coating, a clay-like material with formula [$Mg^{2+}_{1-x}(Al^{3+}/Rh^{3+})_x(OH^-)_2][NO_3^-]_x \cdot nH_2O$, on the working electrode of a three-electrode cell.

This electrochemical deposition process can be applied to coat metallic foams; in this case, a FeCrAlY-alloy was chosen as working electrode. The resulting foam is coated with a thin film of hydrotalcite, which after calcination forms a catalyst

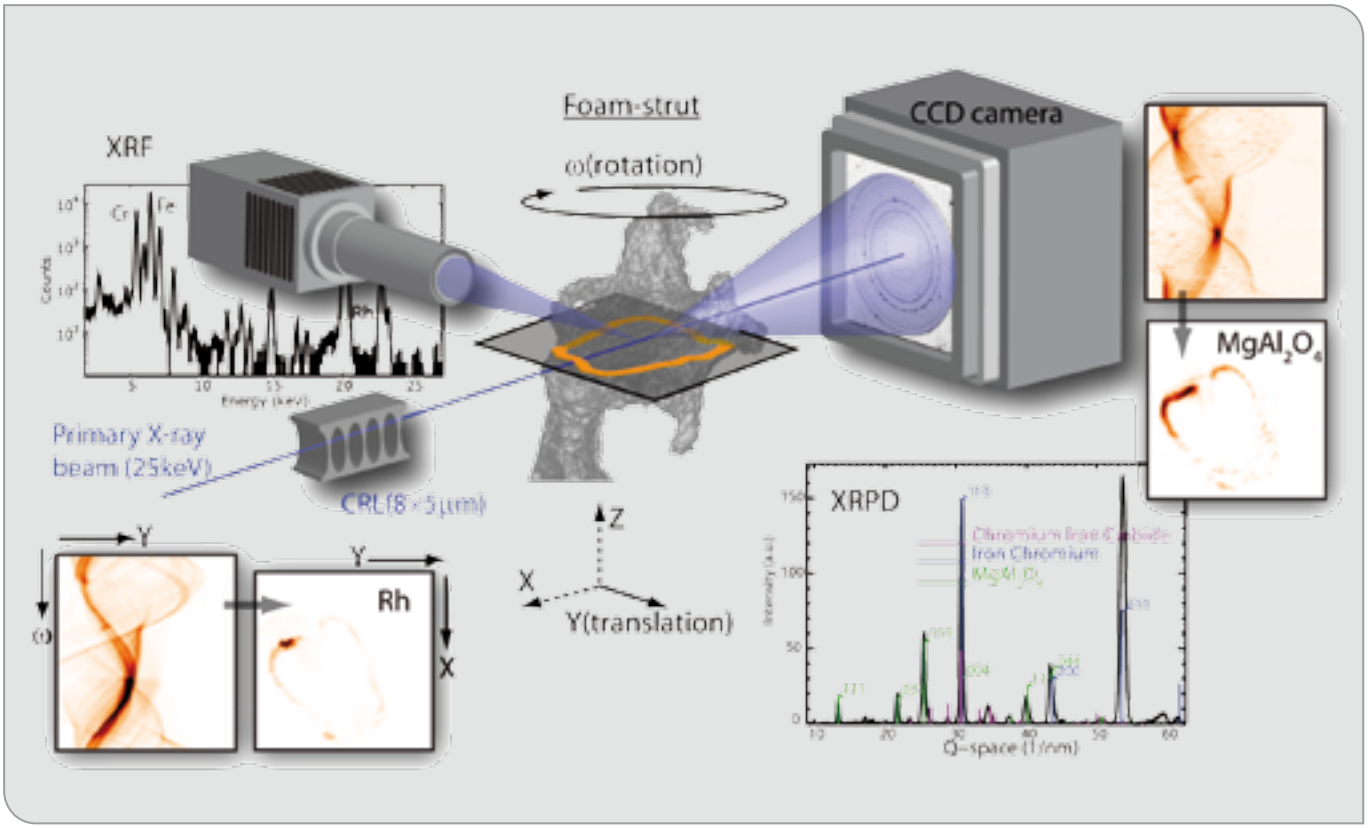

Figure 2:
Combined µ-XRF/µ-XRPD tomography at the FLUO beamline. Element and crystal phase distributions in a virtual cross-section of the coated foam are reconstructed.

that is ready for use („State A"). In a reactor, the catalyst has to be activated by reducing it with hydrogen, after which it can catalyze the conversion of methane and water to syngas (H_2 + CO) (which will be processed further in the water-gas shift reaction). The used catalyst will be referred to as „State B".

To assess the quality of the ECD process and the stability of the catalyst coating under the severe SR conditions, foams in „State A" and „State B" are investigated by a combined micro-X-ray Fluorescence (µ-XRF) and micro-X-ray Powder Diffraction (µ-XRPD) tomography experiment as represented in Figure 2. A strut from the foam will be translated (Y) and rotated (ω) in a microfocussed X-ray beam. An energy dispersive detector collects fluorescence spectra for each translation and rotation step, while an area detector registers diffraction patterns. From the XRF spectra it is possible to extract a signal proportional to the amount of each chemical element present in the material, as a function of Y and ω. The result is called a sinogram and can be transformed into an element distribution map (XY), as illustrated in Figure 2 for Rhodium (bottom-left). This map visualizes the distribution of, in this example, Rhodium in a virtual cross-section of the foam strut. From the diffraction patterns, an analog result can be obtained for crystalline phases, as illustrated in Figure 2 for magnesium-aluminum spinel ($MgAl_2O_4$, top-right). While XRF tomography is a known technique, XRPD tomography only became feasible in recent years, partially due to the development of dedicated software packages like XRDUA, that implement flexible diffraction pattern modeling and tomographic reconstruction.

This technique has been applied on several ECD synthesized catalysts in State A and State B, from which two are shown in Figure 3. The RGB images on the top give an impression on what foam and coating look like in cross-sectional view. The foam itself contains iron, so it can be visualized using the Fe fluorescence signal, as shown in blue. Since the iron fluorescence photons have a relatively low energy, only photons generated on the outside border of the foam strut are visible and a

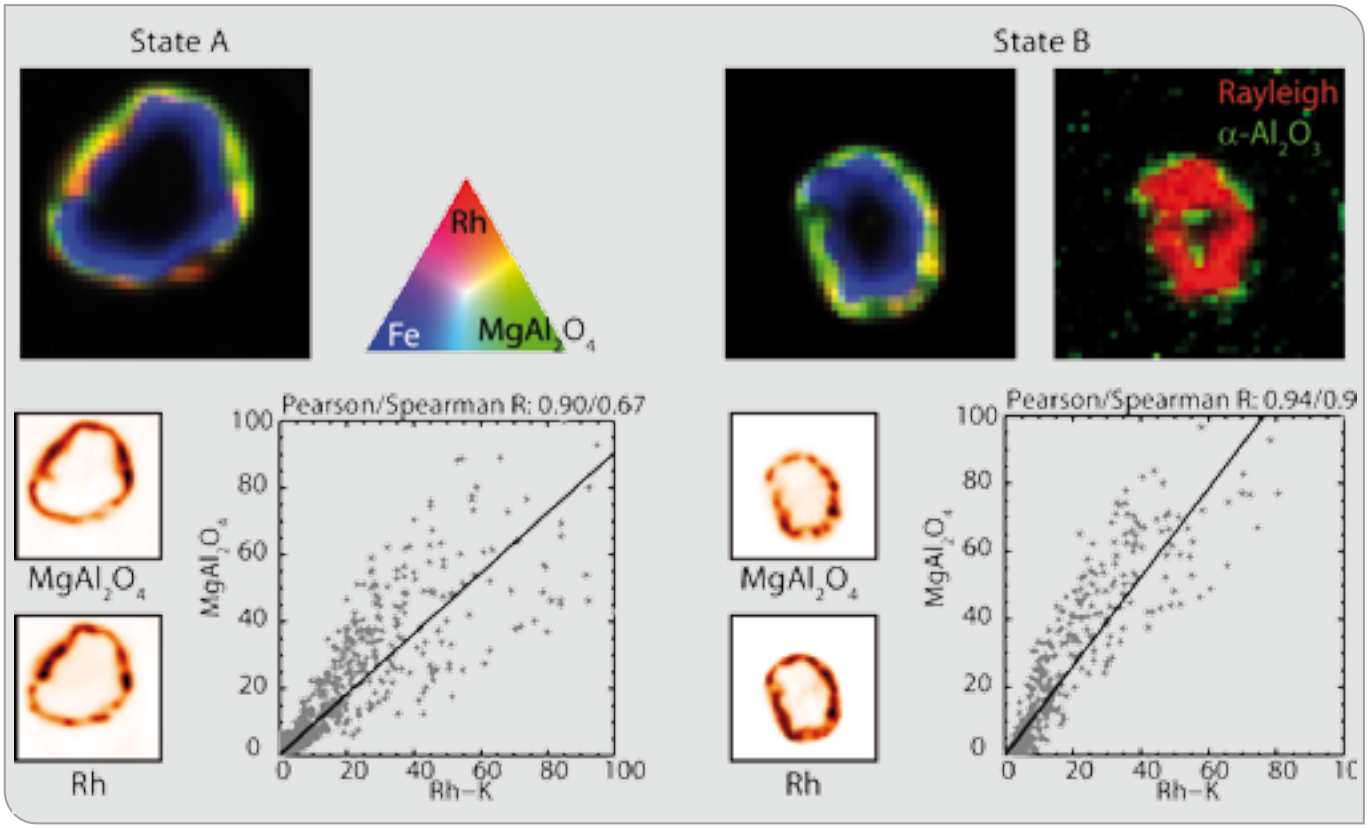

Figure 3:
Virtual cross sections of 123×123 µm² through a catalyst sample before (state A) and after use (state B). Correlation between Rhodium and $MgAl_2O_4$ is shown for both states; the Fe distribution is used to highlight the outside border of the FeCrAlY- foam.
The intermediate corundum layer (α-Al_2O_3) was only just visible in state B at the surface of the foam material;
the Rayleigh scatter peak intensity (visible in the XRF spectra) is used to indicate the location of the foam material (showing internal cavities.

gap appears in the middle. To visualize the inner foam structure, the elastically scattered photons can be used since they retain the initial photon energy of 25 keV and can escape easily from the strut which has a diameter of about 100 µm. An example is given in Figure 3 (top-right, in red) which indicates that there are cavities inside the foam structure.

The coating applied on the foam contains Rhodium (red) and a magnesium-aluminum spinel ($MgAl_2O_4$, green). On some but not all struts in State A and B, an additional layer of corundum (α-Al_2O_3) is just visible. This crystalline phase is not only visible on the outside border of the foam but also on the inside cavity walls (Figure 3, top-right). This happens because the corundum layer is not applied by ECD but is created during the calcination step (see Figure 1) by the oxidation of the aluminium in the foam itself. The Rhodium, which is the catalytically active phase, seems to be colocalized with $MgAl_2O_4$ in State A as well as State B, as evidence by the correlation plots in Figure 3. Previous bulk studies have shown that Rh^{3+} can be included in the spinel structure in State A. In the used State B, Rh^0 particles are supported by or included in the spinel without destroying the structure since the amount of Rhodium used is very low. Although the current experiment does not confirm or reject these previous observations, some conclusions on ECD performance and catalyst stability can be formulated. It is evidenced that the catalytic coating does not seem to detach after performing catalytic tests by comparing the coating thickness and homogeneity in State A and State B. It is also shown that the stability of the catalytic layer is not only mechanically but also chemically determined. The Rhodium catalyst is included in a spinel structure which is bond to aluminum oxide. Both crystalline phases are grown in the same calcination step, the spinel from the hydrotalcite coating and the aluminium oxide from the aluminium containing foam, thus ensuring a strong adhesion between catalyst and support. Finally the ECD process proved to from thin coatings which cover the foam walls relatively homogeneous compared to coatings applied by traditional wash-coating as illustrated in previous studies.

Chemical and mineralogical characterization of aerosol particles from Beijing as an essential contribution to source identification and health risk assessment

Nina Schleicher[1)], Utz Kramar[1)], Stefan Norra[1),2)], Volker Dietze[3)], Uwe Kaminski[3)]

1) Institute of Mineralogy and Geochemistry, Karlsruhe Institute of Technology, Karlsruhe, Germany
2) Institute of Geography and Geoecology, Karlsruhe Institute of Technology, Karlsruhe, Germany
3) Research Center Human Biometeorology, Air Quality Department, German Meteorological Service, Freiburg, Germany

Figure 1:
Dust storm day in Beijing (Forbidden City, photo: Chen Yizhen).

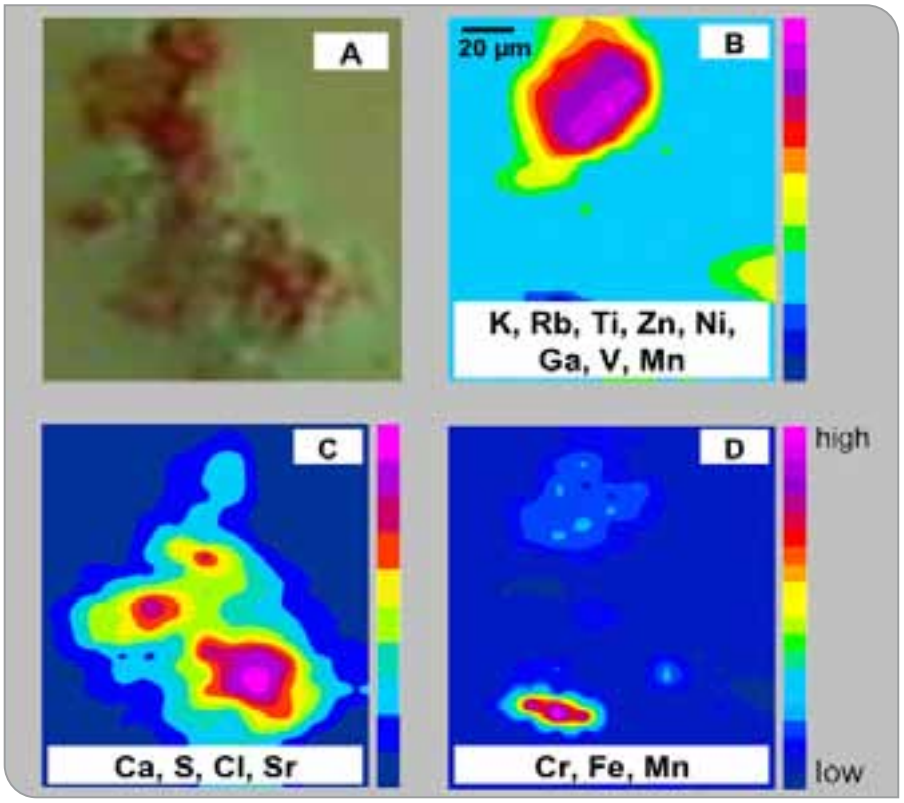

Figure 2:
Agglomerated dust particle from Beijing.
A: Microscopic image,
B-D: The three groups represent parts with different composition based on factor analysis carried out with results of µ-SXRF measurements.

Beijing, the capital of China and host city of the Olympic Games 2008, is suffering from severe aerosol pollution. The megacity Beijing (15 million inhabitants) accounts to one of the most polluted cities in the world. Air pollution increases the number of respiratory and/or cardiovascular diseases. Besides numerous anthropogenic sources, additionally geogenic coarse atmospheric particles contribute to the overall pollution especially in spring, e.g. transport of dust from western deserts towards the megacity (Figure 1).

Although a huge knowledge already exists on atmospheric particulate pollution, only very limited knowledge is available on mineral and chemical composition of single atmospheric particles. Especially, the micro-scaled elemental composition of single atmospheric particles and the agglomeration processes of fine anthropogenic and highly toxic particles with coarse geogenic and less toxic particles were not yet investigated in detail. Coarse particles act as sinks for finer particles. In Asian cities, where coarse particles play an important role in overall air pollution, it is essential to clarify this role of large particles as "catcher" for smaller ones. Moreover, the influence of coarse atmospheric particles on the weathering of buildings is an important aspect for urban areas. Stone decay of monuments is favored by wet and dry deposition of atmospheric particles. Often the formation of salt efflorescence, e.g. sulfates, plays a decisive role for the soiling of buildings. Therefore, also particles with salt coating were investigated more closely.

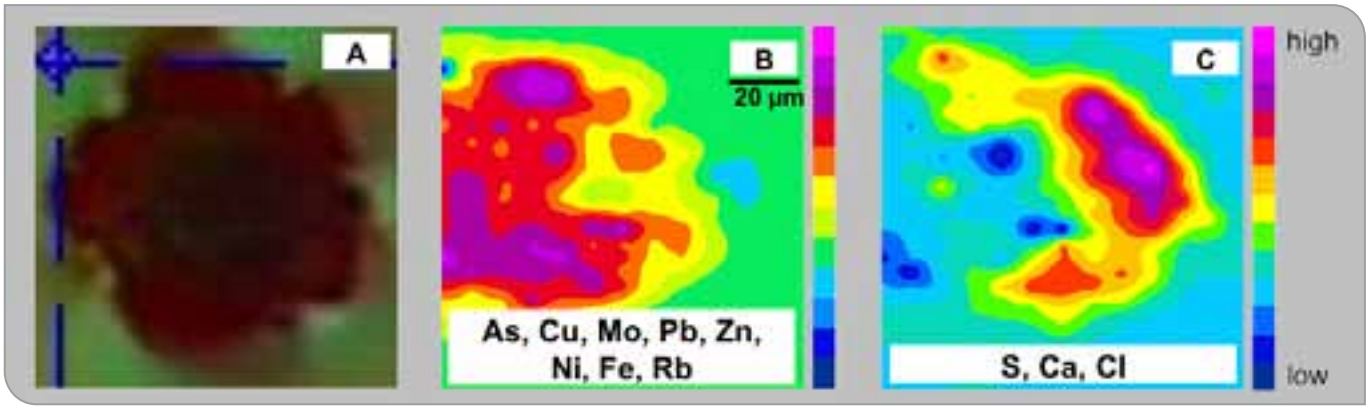

Figure 3:
Dust particle with sulfate coating from Beijing.
A: Microscopic image,
B,C: The two groups represent parts with different composition based on factor analysis carried out with results of µ-SXRF measurements.

On the one hand, coarse particles were passively collected in Beijing on transparent adhesive collection plates with the Sigma-2 sampling device. Several particles were analyzed with regard to their elemental distribution by means of synchrotron radiation based X-ray fluorescence analysis (µS-XRF) at the FLUO-beamline at ANKA. On the other hand, actively sampled TSP (total suspended particles) were collected on quartz fibre filters. The mineralogical composition of the filter samples was analyzed by synchrotron radiation based X-ray diffraction (µS-XRD) at the SUL-X-beamline at ANKA.

The particles analyzed by µS-XRF were inhomogeneous with regard to their chemical composition. Figure 2 shows an example of a coarse agglomerated particle (A). Here, three major parts could be distinguished by factor analysis based on measured element mappings (Group B – D). Group B combines typical crustal elements (K, Rb, Ti, Zn, Ni, Ga, V, Mn) and can be interpreted to stand for a silicatic particle. Group C represents a carbonaceous particle with elements such as Ca, S, Cl, Sr. Very high concentrations of Cr and Fe were found in a small particle within the agglomerate (Group D), probably representing a small toxic anthropogenic particle. An example of a particle with a sulfate coating is shown in Figure 3.

Analysis of mineralogical composition by µS-XRD showed high gypsum concentrations in Beijing dust. A main source for those particles was assumed to be construction activities. Constructions sites are abundant in Beijing and were intensified in preparation of the Olympic Games in summer 2008.

The combination of µS-XRF and µS-XRD analysis showed strong anthropogenic input from a variety of sources, such as traffic, industry, coal burning and intensive construction activities. Moreover, geogenic sources such as long-range transport of dust from arid areas and deserts (e.g. Gobi desert) into the city of Beijing, contributed to the overall air pollution. Agglomeration of fine dust on bigger particles seems to be one of several mechanisms having an impact on dust deposition.

The study demonstrated that the synchrotron radiation facility at ANKA is an excellent tool to study dust particles more closely in order to gain detailed knowledge, which is important for the source identification and health risk assessment of atmospheric particles. In future, these investigations will be continued with regard to seasonal variations and to evaluate effects of the reduction measures applied by the Chinese Government beginning in August 2008 during the Olympic Games.

More detailed results of this study can be found on the CD and in the „Instrumentation Book".

Identification of structural defects in 4H-SiC Material and Devices

B. Kallinger[1)], S. Polster[1)], P. Berwian[1)], J. Wittge[2)], A.N. Danilewsky[2)]

1) Fraunhofer IISB, Dept. Crystal Growth, Schottkystr. 10, 91058 Erlangen, Germany
2) Crystallography, University of Freiburg, Hermann-Herder-Str. 5, 79104 Freiburg, Germany

4H-Silicon Carbide (SiC) is an important semiconductor material which is exceptionally well suited for high power and high voltage applications (e.g. power converters) due to its intrinsic material properties. However, state of knowledge is that the performance of some SiC-based devices (bipolar diodes used at blocking voltages above 2000V) may be limited by certain structural defects in the material. This currently retards the commercialisation of such devices. The aims of our studies performed at ANKA were to identify the structural defects present in the material at different stages of the device manufacturing process, to verify if a characterization method which is more accessible than synchrotron topography is useful for process optimization, and to investigate the effect of device operation on the defect content within the device.

SiC bipolar devices (diodes) are manufactured on SiC wafers. On such a wafer, epitaxial SiC layers are deposited by chemical vapour deposition. These layers are further processed to the device structures. One crucial step of this whole manufacturing process, with regard to material defects, is the deposition of the epitaxial SiC layers. These defects, so-called dislocations, already exist in the 4H-SiC single crystalline substrate and typically propagate into the homoepitaxial layer during its deposition.

In the active area of devices a certain type of dislocation can trigger the formation and expansion of further defects (stacking faults) which are harmful to the long-term stability of bipolar devices. The strategy to improve the stability of bipolar devices is to avoid this certain type of dislocations in the active area of the device and hence the degradation mechanism. Other defects are probably not harmful for the long-term stability of bipolar devices.

It is very difficult to remove dislocations from the substrate material. Therefore, the most promising strategy to overcome this problem seems to be to avoid the propagation of the most problematic defects from the substrate into the epitaxial layers.

X-ray topography (XRT) at ANKA was the ideal characterization tool for this task, because it allows for the imaging of dislocations and identification of their types on relatively large areas of SiC wafers. Moreover, it is a non-destructive method; material can be characterized at different stages of the device manufacturing process without influencing the further processing steps. We designed our ANKA experiments according to three main issues: Firstly, we wanted to identify every single dislocation present in certain areas of the substrates before epitaxy, and in the corresponding epitaxial layers grown on these substrates. Certain dislocation reactions can take place during the manufacturing, e.g. a conversion of so-called Basal Plane Dislocations (BPDs) into other dislocation types. How can these reactions be used to improve the material quality?

Secondly, we wanted to qualify the standard method of dislocation identification of SiC substrates and epilayers: Defect Selective Etching (DSE). During etching of the material, small pits are formed where the dislocations intersect the surface of the wafer. As DSE detects dislocations indirectly, this method has to be verified with respect to the accurate determination of the dislocation density and the interpretation of different etch pit types. Is the standard method of defect identification valid in all cases?

Thirdly, XRT was applied to reveal the defect content within the active area of bipolar devices after operation. By these investigations we wanted to analyse how the defect content in devices correlates with the device operation. Do we find a way to avoid device degradation?

In replay of the scientific questions:

1. Identification of dislocation types in 4H-SiC substrates and epitaxial layers and dislocation reactions

Dislocations present in substrates and epitaxial layers were investigated at ANKA. The beam time was split into two sessions. The first session was dedicated to dislocations in substrates, the second session addressed the dislocations in homoepitaxial layers grown on the substrates of the first session.

All measurements were performed at the TOPO-TOMO beam line in back-reflection geometry to image exclusively dislocations near the sample surface. Type and propagation direction of each dislocation were determined. We found all types of dislocations already discussed in literature. So-called Threading Dislocations of screw (TSD) and edge (TED) type as well as BPDs were found both in substrates and epilayers. Surprisingly, besides these well-known dislocation types in 4H-SiC, we found other types

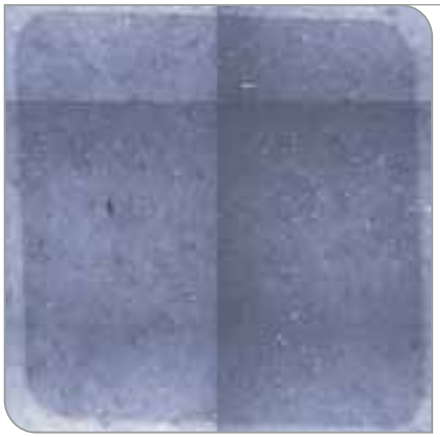

Figure:
Synchrotron X-ray topograph of a bipolar diode before electrical stressing.

Topograph was taken at ANKA in back-reflection geometry with g = 0001. The darker area corresponds to the active area of the device. Large white spots represent Threading Screw Dislocations (TSD).

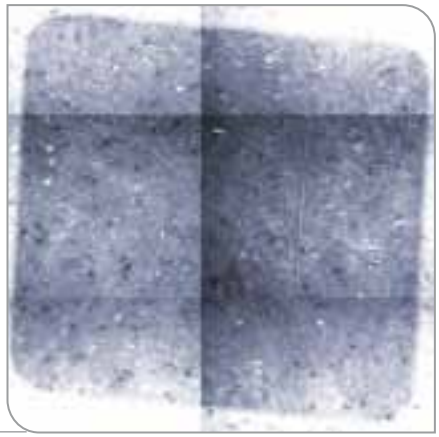

Synchrotron X-ray topograph of an electrically stressed bipolar diode stacking faults (straight white line).

of dislocations. They behave quite similar to TEDs but deviate from "normal" TEDs with respect to their visibility characteristics in the XRT as well as etching behaviour. It should be interesting to see if these defects show a different electrical behaviour when compared to the known TEDs. The structure of these dislocation types will be further investigated by XRT in grazing-incidence geometry.

Dislocation behaviour during epitaxial growth was investigated by comparison of the dislocation pattern of substrates and the epilayers grown on top of them. It was found that all threading dislocations (TSD and TED) propagate to the epitaxial layer without any change of their growth pattern. However, BPDs from the substrate are able to convert to TEDs during growth. Hence, the total dislocation density remains constant during epitaxial growth, but the number of BPDs in the layer can be reduced due to conversion to TEDs. BPDs are considered to be the only dislocations which may harm device stability. By the ANKA analyses we were able to show that our epitaxial process allows for an exceptionally good BPD conversion rate.

2. Verification of the defect selective etching method with respect to dislocation identification

The characterization method of defect selective etching was verified with help of the XRT method. The etch patterns were compared to the dislocation patterns (obtained by XRT) for each sample in order to find corresponding dislocation contrasts and etch pits. A 1:1 correlation of etch pit and dislocation was found for all samples, indicating that the etch pit density equals the dislocation density at the sample surface. The etching method is therefore valid for assessing the overall dislocation density of a sample.

For n- and p-type samples with different doping levels throughout the maximum doping range, the etch pits were correlated to the dislocations types. Detailed results of this study are submitted to Journal of Crystal Growth for publication. The results were presented as posters at the annual ANKA users' meeting 2009 in Karlsruhe and at the International Conference on Silicon Carbide and Related Materials (ICSCRM 2010) in Nuremberg. Both presentations were awarded as the best student's poster. Sebastian Polster received the Hugo-Geiger-Prize 2010 of the Fraunhofer society for his diploma thesis about defect analysis by means of defect selective etching, x-ray topography and x-ray diffraction. In short, identification of the different dislocation types is not unambiguous in all cases and careful interpretation of the etching results is needed. E.g. in case of heavily N-doped substrates, it is not possible to distinguish TEDs or TSDs.

3. Defect content in bipolar diodes

A total of 11 bipolar diodes were investigated with back-reflection XRT to reveal their defect content in the active area of the devices and to compare the occurrence of so-called stacking faults to the electrical characteristics of these diodes. Some of these devices were electrically stressed to activate defect reactions (e.g. the formation and expansion of stacking faults), others were unstressed.

None of the unstressed diodes contained stacking faults, but some of the stressed diodes exhibited one or two stacking faults. This supports the pertinent model of defect behaviour during operation. A larger number of electrically stressed bipolar diodes must be investigated to ensure that the degradation of bipolar diodes is overcome in case of state-of-the-art bipolar diodes.

Conclusions

The XRT investigations performed at ANKA are an important contribution to the progress in science and the development of innovative SiC electronics. Such investigations are dependent on XRT due to its characteristic feature of defect identification on large areas.

The distribution of important bio-metals and the determination of Fe, Cu and Zn oxidation state in breast tumour tissue using μSRXRF and XANES Techniques

M.J.Farquharson[1)], A.Al- Ebraheem[1),2)]

1) Department of Medical Physics and Applied Radiation Sciences, McMaster University, 1280 Main St. W. Hamilton, Ontario, Canada, L8S 4L8.
2) Department of Radiography, School of Community and Health Sciences, City University, London, EC1V 0HB, UK

Excessive accumulation of Cu, Zn and Fe in breast cancer compared to normal breast tissues has been reported in a number of studies. The observation of such differences in bulk samples has in the last few years been followed up by small beam imaging that allows metal levels to be mapped across a specimen revealing preferential sites of accumulation. During this work on breast cancer tissue using mapping technique, elemental maps at micron-scale from a substantial number of specimens were collected at the FLUO Beamline at ANKA aiming to associate the metal distributions to physiological parameters that influence disease progression and response to treatment. Furthermore, X-ray absorption near edge structure (XANES) spectroscopy was utilised using the SUL-X Beamline at ANKA, to identify the oxidation state of Zn, Fe and Cu in normal and tumour breast tissues in order to correlate the oxidation sate of these elements to the carcinogenesis process.

Cellular concentrations of zinc, one of the metals of physiological importance in many processes, are strictly regulated by a number of zinc transporter proteins. A subset of these proteins has been shown to be regulated by oestrogen, a hormone that is heavily involved in the progression of the disease. It is documented that many treatment regimes are preferentially effective in treating oestrogen receptor positive (ER +ve) tumours in contrast to oestrogen receptor negative (ER –ve) ones. In this context the present study investigated the zinc levels in human primary invasive breast carcinoma (Farquharson et al 2009).

The samples were in this case classified based on their oestrogen receptor status. Eighteen such specimens were mapped on this occasion, subset of a total of 59 measured at three different synchrotrons. The maps obtained reveal the accumulation of the metal in the invasive tumour areas. For the statistical analysis, regions of tumour and normal tissue were selected in each sample and the normalised zinc signal from each was then calculated.

For each specimen the levels of zinc in the cancerous parts were statistically compared with that of the surrounding normal tissue and that parameter was then correlated to the ER status of patients. While the metal is always found to be elevated in the tumour areas in relation to the normal tissue surrounding it, this contrast is much more marked for the ER +ve cases.

The results from this study have led us to the next set of investigations which is already under way. The zinc content was evaluated in 50 specimens from patients that have been treated with tamoxifen and further categorised in terms of response to such treatment. This work is part of an extensive trial (Adjuvant Breast Cancer (ABC) trial) encompassing a number of countries and methods of investigation therefore these results can be used to aid elucidation of the variable effectiveness of tamoxifen in the treatment of such cases.

A micro-mapping of trace elements distribution in breast tissues was performed at the FLUO Beamline at the energy of 10 keV. X-ray fluorescence radiation is collected using an energy dispersive Si (Li) solid state detector. A 45^0 geometry was used between the incident radiation beam and the sample, and a 90^0 geometry between the incident beam and the detector.

The samples were in the form of tissue micro arrays consisting of 1.0 mm diameter sections of tissue microtomed to slices 10 microns thin. Stained H&E histology sections adjacent to those imaged on the beamline were used to guide the selection of scanned regions. For more information about sample preparation, experimental parameters and analysis see (Farquharson et al 2009).

During the beamtime a large on sample spot size of approximately 25μm x 15μm was used to scan samples with well differentiated ROIs (see Figure 1). While, to scan samples less differentiated ROIs at high resolution, a small on sample spot size of approximately 5μm x 5μm was used (see Ffigure 2).

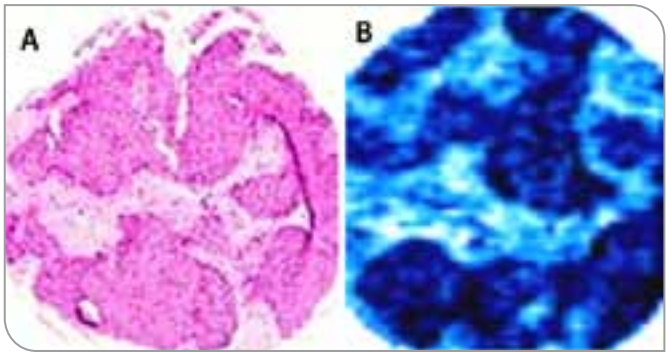

Figure 1:
A) H&E stained reference sample, B) Zinc distribution map.

The dark areas are the tumour cells whereas the lighter areas are normal tissue. ROI 900 x 900 µ, beam size of 25 x 15 µ.

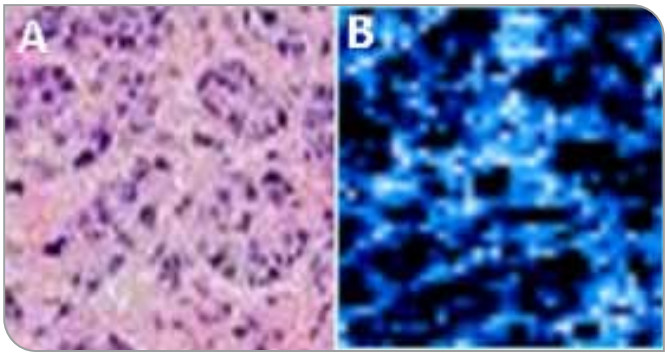

Figure 2:
A) H&E stained reference sample, B) Zinc distribution map.

The dark areas are the tumour cells whereas the lighter areas are normal tissue. ROI 200 x 200µ, beam size of 5 x 5 µ.

A similar experimental setup was used to collect the XANES data at the SUL-X beamline which has a Wiggler radiation source. The oxidation states of Zn, Cu and Fe were determined by comparing the XANES spectra from each element with standard chemical compounds of these elements. For more information about XANES experimental parameters and analysis see (Al-Ebraheem et al 2010).

The results have shown that the mean total Zn content for each sample (i.e. tumour and surrounding regions) was approximately 60% higher in the ER +ve samples than that in the ER –ve samples (Farquharson et al 2009).

The results of investigating the levels in a specific group of breast cancer patients treated with tamoxifen have shown that Zn levels were significantly higher in the relapsed tumour status than that in the non relapsed tumour status. We are currently still working on this data and planning further studies.

The results of investigating the oxidation state of Cu, Fe and Zn in the breast tissue using XANES suggested that iron is shifted toward Fe (III), Zn exists in bounded form Zn (II), and a significant portion of the total copper is present as Cu (I), in the normal and the tumour tissues. The data from the experiment has been accepted for publication (Al-Ebraheem et al 2010). Figure 3 shows the average spectra of all normal and tumour tissue samples and the reference materials of Zn. The position of the Zn K-edge remains almost identical for all normal and tumour tissue samples. The position of the edge suggests that Zn exists as bounded form (Zn (II)).

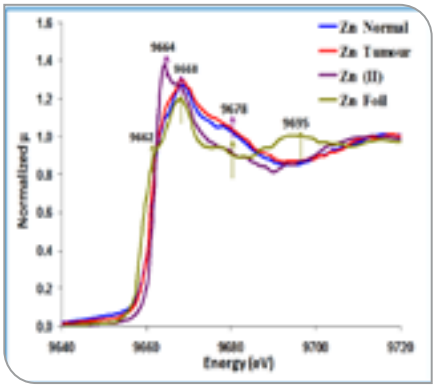

Figure 3:
Comparison of the Zn K-edge XANES spectra obtained for average normal and tumour tissues and for the reference materials.

Conclusion and Outlook

These results suggest that increased intracellular Zn levels can be used as a predictor of tamoxifen failure in treated carcinomas. Because of the large number of variables involved in the trial data, more cases from the ABC trial samples have been scanned in order to obtain significant data to complete this study.

The determination of any alteration in the Fe (II)/Fe (III) and Cu (I)/Cu (III) ratio and the distribution of Fe and Cu oxidation states within the tumour and normal cells could be used as oxidative markers. Further analysis will be carried out to demonstrate how Fe (II), Fe (III), Cu (I) and Cu (II) are distributed throughout the tissue.

Facts and Figures

Machine Operation

The storage ring is generally operated at energy of 2.5 GeV with a typical beam current of 200 mA and a lifetime of around 20 hours. In dedicated shifts, beam is provided at 1.3 GeV for deep X-ray litho-graphy (to obtain a soft spectrum) and infrared applications (to operate at shortest bunch length).

From July 2009 to June 2010, the storage ring has been in operation for 4590 h: 3959 h at 2.5 GeV (whereas 3328 h for user operation) 359 h at 1.3 GeV mainly for coherent IR radiation, 274h at 0.5 GeV (mainly used for injection). Per month about 142 days are dedicated for user operation, 45 days for Special User Operation and 41 days for start up and machine physics Studies (Figure 2).

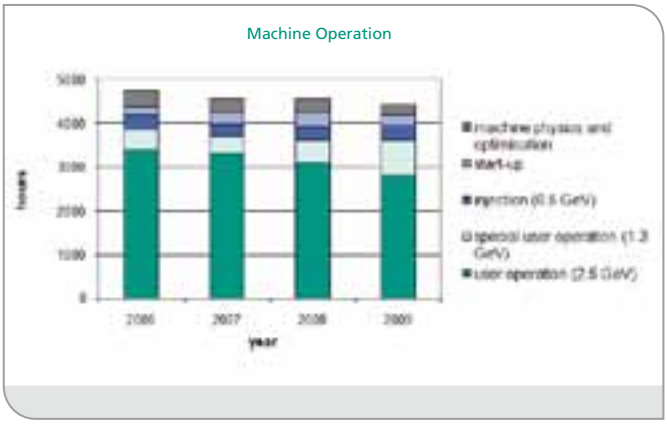

Figure 1: Machine operation 2006 - 2009.

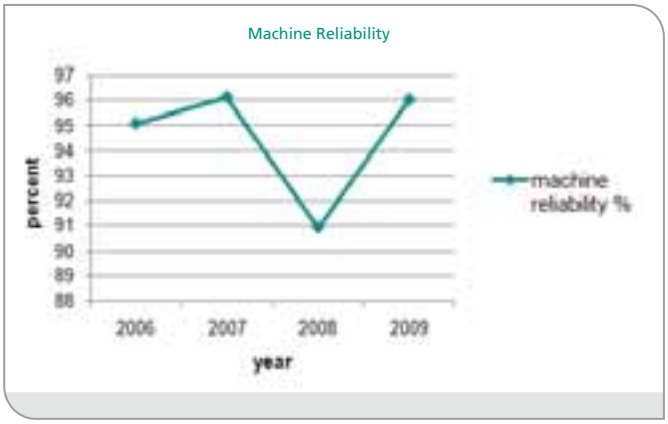

Figure 2: Experiments of the 15th call by scientific area.
(The ration between scheduled and delivered beam time is typically 96%)

User Operation

Synchrotron light from the ANKA facility is available for use by the national and international scientific community. About eight hundred users from 16 different countries have been involved in the 14th and 15th Call (October 2009 until September 2010).

Figures 1 and 2 present the regional origin of home institutions of participating scientists. Figures 3 and 4: illustrate the break-down of experiments by scientific area.

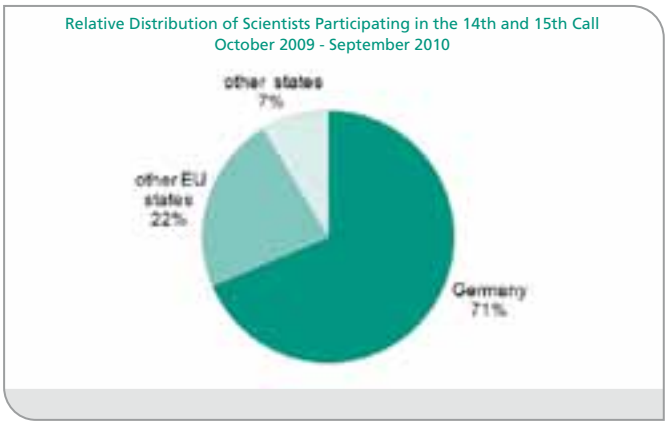

Figure 1: Distribution of countries of the home institutions of ANKA users.

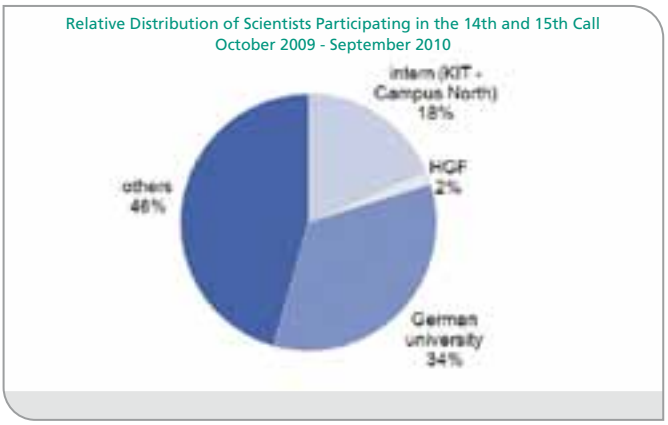

Figure 2: Distribution of the home institutions of ANKA users of Germany.

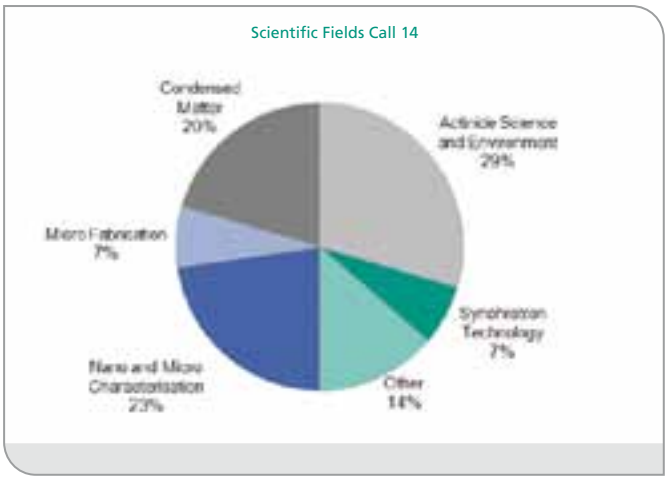

Figure 3: Experiments of the 14th call by scientific area.

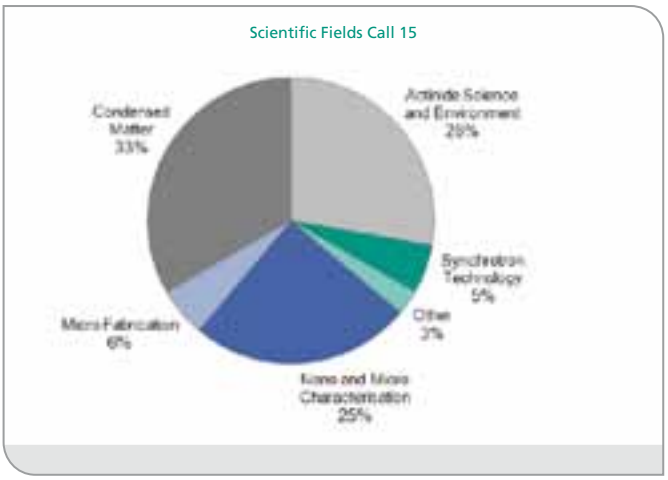

Figure 4: Experiments of the 15th call by scientific area.

ANKA Beamlines

Experimental competences available at ANKA's beamlines can be divided as follows: X-ray Spectroscopy, X-ray Scattering & Imaging, Infrared Spectroscopy, and X-ray Lithography. Presently, there are fourteen beamlines in operation supplemented by laboratory infrastructure for experimental methods complementary to those available at the beamlines (UHV lab, Chemistry lab, Laser lab, Femto lab, and MOVPE lab). In 2011 NANO beamline will go into operation, IMAGE beamline is under construction, and the CAT-ACT beamline for heterogeneous catalysis and actinide research is in the planning stage. Table2 gives an overview of existing ANKA's beamlines and those foreseen to be in operation in 2011.

More information about beamlines and labs at ANKA can be found in the Instrumentation Book. Five beamlines are operated as CRG instruments (see Table 1).

Beamlines	Labs
LIGA I, II and FELIG	KIT - IMT, Institute for Microstructure Technology
WERA beamline	KIT - IFP, Institute for Solid State Physics
INE beamline	KIT - INE, Nuclear Waste Disposal
UVCD/CD12 beamline	KIT - IBG, Institute for Biological Interfaces
MPI-MF beamline	MPI - MF, Max Planck Institute for Metals Research

Table 1: Beamlines operated by other institutes

Figure 1: Installation of the new diffractometer for the NANO beamline

Figure 2: „in-situ X-ray diffraction measurement during Argon arc-welding of a steel plate. The 2 X-ray detectors are located above and below right in the image, the X-ray beam enters from the tube on the right, and the sample/welding electrode are left of centre"

Beamline	Technical and schematic application	Experimental station	Specification	Source	Status
FLUO	X-ray fluorescence analysis (XRF), X-ray fluorescence microprobe (μ-XRF), total X-ray reflection fluorescence (TXRF)	Vacuum chamber, SiLi-detector	Energy range: 1 - 30 keV Resolution: $2x10^{-2}$ ΔE/E	Dipole magnet	Operational
XAS	Extended X-ray absorption fine structure (EXAFS) X-ray absorption near edge fine structure (XANES), Q-EXAFS	Ionization chambers, 5 element Ge detector, closed cycle He cryostat, 4 axis goniometer for GI-XAFS	Energy range: 1 - 30 keV Resolution: $2x10^{-2}$ ΔE/E	Dipole magnet	Operational
INE	Spectroscopy of actinide samples	Ionization chambers, 5 element Ge detector, 4 axis goniometer for GI-XAFS, liquid N cryostat Vortex silicon drift detector	Energy range: 2.1 - 25 keV Resolution: $2x10^{-4}$ ΔE/E	Dipole magnet	Operational
SUL-X	X-ray diffraction (XRD), X-ray-fluorescence spectroscopy (XRF) and X-ray absorption spectroscopy in μ-focus	Vacuum chamber, ionization chambers, 7 element SiLi-detector, 4 axis diffractometer + CCD detector	Energy range: 1.5 - 20 keV (presently 2.14 – 20 keV) Resolution: $2x10^{-4}$ ΔE/E (for Si crystals)	Wiggler	Operational
WERA	Soft X-ray spectroscopy, microscopy, and spectromicroscopy: PES, NEXAFS, SXMCD imaging (PEEM); μ-PES, μ-NEXAFS, μ-SXMCD	3 experimental chambers w/ associated preparation chambers, all UHV. PEEM, electron energy analyzer, fluorescence detector, LHe cryostats, UHV sample transfers	Energy range: 100 – 1500 eV Resolution: E/ΔE up to $1x10^{4}$	Dipole (present); dipole and undulator (future)	Operational
IR 1	Infrared/THz spectroscopy and ellipsometry	FTIR spectrometer, ellipsometer, liquid He cryostats	Spectral range: 4 - 10000 cm^{-1} Best spectral resolution: 0.1 cm^{-1}	Dipole magnet edge	Operational
IR 2	Infrared/THz, spectroscopy, microscopy, imaging and near field nanospectroscopy	FTIR spectrometer, IR microscope, IR nanoscope, liquid He cryostat	Spectral range: 4 - 10000 cm^{-1} Best spectral resolution: 0.1 cm^{-1} Spatial resolution: diffraction limited (microscopy), 100-1000x beyond the diffraction limit (nanoscopy)	Dipole magnet edge	Operational 2009
CD 12	Soft X-ray spectroscopy and microscopy, photoelectron spectroscopy, SXMCD	PEEM, fluorescence detector, electron energy analyzer, SXMCD setup, cryostat, preparation chambers including pulsed laser deposition, UHV	Energy range: 100 – 1500 eV Resolution: up to $1x10^{-4}$ ΔE/E	Dipole (present); dipole and undulator (future)	Operational by the end of 2010

Beamline	Technical and schematic application	Experimental station	Specification	Source	Status
PDIFF (upgraded)	X-ray powder diffraction (XRPD), roentgenography, single-crystal diffraction	4+2 circle diffractometer	Energy range: 6 - 20 keV Resolution: $2x10^{-4}$ ΔE/E	Dipole magnet	Operational
SCD	Single crystal diffraction, SAD/MAD, ex-situ characterisation of (nanostructured) surfaces and interfaces with XRD, XRR, GID, GISAXS	3 axis diffractometer with CCD-detector and 2 axis diffractometer with image plate detector, 6 axis diffractometer with PSD and with YAP and NaI point detectors	Energy range: 4 - 20 keV Resolution: $3.5x10^{-4}$ ΔE/E	Dipole magnet	Operational
NANO	X-ray diffraction (HR-XRD) with highest angular resolution, anomalous scattering, coherent scattering	Multi purpose heavy duty diffractometer; different growth chambers; cryostat; furncase	Energy range: 3 keV – 25 keV Resolution: 10^{-4} to 10^{-2} ΔE/E	Super-conducting undulator	In Commission
MPI-MF (MPG)	Surface diffraction, XMCD	2+3 circle horizontal and vertical diffractometer for high load (300 kg)	Energy range: 5 - 20 keV Resolution: $2x10^{-4}$ ΔE/E	Dipole magnet	Operational
TOPO-TOMO	Topography, Tomography, Radiography	4 axis goniometer, tomography stages, stages for 300 mm wafer	White beam, optional 10^{-2} ΔE/E (2008)	Dipole magnet	In Commission
IMAGE	Radiography and tomography	Ultra-precise sample manipulator; automatic sample changer system. 2D detector system; energy-dispersive detector	Energy range: 7 keV- 65 keV Resolution: 10^{-2} to 10^{-4} ΔE/E	Super-conducting combined wiggler/ undulator	Under Construction
LIGA I	Mask fabrication, patterning of thin microstructures	Scanner	Energy range: 2.2 – 3.3 keV	Dipole magnet	Operational
LIGA II	Deep X-ray lithography	Scanner	Energy range: 2.5 – 12.4 keV	Dipole magnet	Operational
LIGA III	Ultra deep X-ray lithography	Scanner	Energy range: 2.5 keV upwards	Dipole magnet	Operational

Table 2 (left and right): Operational and planned beamlines and experimental stations
(red: spectroscopy beamlines, green: scattering and imaging beamlines, blue: beamlines for microfabrication).

Public Activities -
Conferences, Meetings and Workshops

Joint QUASAR and THz-Groups Workshop on „Accelerator Science and Technology“

Organized by:	FZK-ANKA
Date:	September 6 - 10, 2009,
Venue:	Hohenwart Forum Pforzheim
Participants:	approx. 30

After the successful workshop in Bad Herrenalb 2008, the QUASAR and THz-Groups joined forces again to organize a workshop on “Accelerator Science and Technology” in Pforzheim, Germany.

Cutting edge developments in the field of particle accelerators formed again the focus of the discussions during the four days, but also complementary skills, such as presentation techniques, project and time management, and feedback were intensely

discussed. POL sessions on cyclotrons, the reaction microscope, spectrometer design, particle beam cancer therapy, beam energy measurements, and the electron cloud effect complemented the workshop program.

During a full day excursion to the Helmholtz Centre for Heavy Ion Research (GSI) in Darmstadt the present R&D program of both groups was presented in 18 talks underlining the broad research spectrum both groups are covering. Drs. Peter Forck and Tobias Hoffmann from GSI’s beam diagnostics groups kindly offered a visit to the GSI accelerator facility and explained details about the future FAIR facility.

ICXOM20 – The 20th International Congress on X-ray Optics and Microanalysis

Organized by:	FZK, European Joint Research Centre (ITU)
Date:	September 15 - 18, 2009,
Venue:	Congress Center Karlsruhe
Participants:	nearly 150

The 20th International Congress on X-ray Optics and Microanalysis, ICXOM20, was hosted by the Research Center Karlsruhe (Forschungszentrum Karlsruhe, FZK, now KIT), Germany, and organized by members of FZK and the European Joint Research Centre Institute for Transuranium Elements (ITU). ICXOM20 was attended by nearly 150 registered participants from 23 different countries around the world, making it truly an international event with a broad range of interesting and exciting contributions. The ICXOM series is dedicated to the fields of X-ray optics and micro (nano) analysis by means of X-ray beams, electrons or other energetic particles. In 2009 emphasis was placed on synchrotron sources.

The oral and poster presentations at the 20th in the Congress series were divided into six general topics:

- Modern micro- and nano-analysis
- Advances in instrumentation, detection, and methodology
- X-ray optics (monochromators & multilayers, focusing optics
- Quantitative and multi-variate analysis
- Imaging techniques and image processing
- Applications of nano-, micro-, and surface analysis techniques

A satellite seminar “Introduction to Synchrotron-based micro (nano) analysis and imaging methods” intended for young scientists with lectures given by internationally renowned speakers was held on September 14, 2009. ICXOM20 participants visited the synchrotron source ANKA on the FZK site during a poster session which was held in the ANKA hall.

1st ANKA/KNMF - Joint User Meeting

Organized by: KIT-ANKA and KIT-KNMF
Date: October 08 - 09, 2009,
Venue: Badnerlandhalle, Karlsruhe
Participants: nearly 170

The Synchrotron Radiation Source ANKA and the Karlsruhe Nano Micro Facility KNMF invited to the 1st Joint Users' Meeting at the Badnerlandhalle Neureut-Karlsruhe.

At the first day the current status of ANKA, the new Karlsruhe Nano Micro Facility and activities of users were presented.

The focus of second day was on scientific issues related to nano and micro characterization & structuring science.

During the two days the ANKA users had the opportunity to meet ANKA and KNMF scientists and discuss about their future projects and past experiences.

The 1st ANKA/KNMF - Joint User Meeting was a great success for all involved partners and participations.

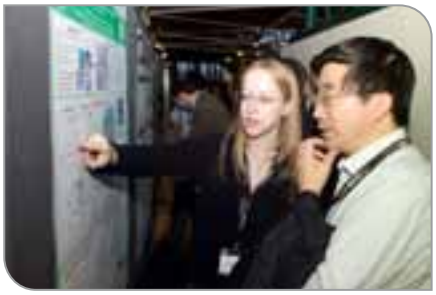

First Meeting of the European Network of Light Source Communicators

Organized by: European Light Sources Activities and KIT-ANKA
Date: November 26 - 27, 2009
Venue: Hotel Residenz Karlsruhe and KIT Campus North
Participants: 17

ANKA is very proud to have hosted the First Meeting of the European Network of Light Source Communicators. The PR-officers of most European light sources came together to discuss maximizing the potential of their facilities and release synenergies by fostering dialogue between science institutions. It was agreed to review the communications practice at each light source facility to find strategies for increasing visibility of the EU-light sources and their scientists.

Scanning and Tomographic Micro-XRD by Means of the XRDU Software Package

Organized by: KIT-ISS-ANKA and Department of Chemistry, University of Antwerp, Belgium
Date: March 23 - 24, 2010,
Venue: KIT Campus North
Participants: 14

Scanning and tomographic micro-X-ray diffraction becomes more and more popular for samples consisting of crystalline material with crystals sizes that are one or two orders of magnitude smaller than the X-ray beam size. Applying these techniques to materials like pigments, catalysts, soils and aerosols results in thousands of two-dimensional diffraction patterns, collected while moving the object under investigation through a focused X-ray beam.

To stay abreast of these changes new software packages are needed for data processing. Wout De Nolf from the Department of Chemistry of the University of Antwerp has developed the XRDUA package for this purposes which he has introduced in the scope of a two and a half days workshop at ANKA covering the following topics:

Session 1: "From raw data to reciprocal space" dealt with correction, calibration and azimuthal integration of raw 2D diffraction patterns. In order words: Converting pixels to d-spacings.

Scanning and Tomographic Micro-XRD by Means of the XRDU Software Package (continuation)

Session 2: "Live at the synchrotron" illustrated how XRDUA can give feedback to the experimentalist during an experiment to check and adapt his experimental design. A tomography scan on a test object has been used as an example.

Session 3: "From reciprocal space to real life" has been about producing the results, emphasizing on crystallographic phase distribution maps (from 2D scanning or tomography). Pigment analysis of a 15th/16th century book of tides illustrated the batch processing capabilities of XRDUA (Pattern decomposition and Pawley fitting). Data from the "IUCr CPD Round Robin on Quantitative Phase Analysis" are taken as a Rietveld refinement exercise.

Wout has done a great job during these two and a half days making us familiar with the huge capabilities of his package. There was also time reserved to get start-up aid from him for own data sets.

Scanning and Tomographic Micro-XRD pilot measurements have been performed so far at the ANKA beamlines FLUO and SUL-X. The INE-Beamline is equipped for such techniques and will perform first scans in July 2010.

THz Radiation: Generation, Detection and Applications (456. WE-Heraeus Seminar)

Organized by:	KIT-ANKA
Date:	April 18 - 21, 2010,
Venue:	Physikzentrum Bad Honnef
Participants:	approx. 25

The Terahertz (THz) range of the electromagnetic spectrum is characterized by a dramatic increase in research and development activities around the world. The THz region of the electromagnetic spectrum - located between millimeter waves and infrared radiation is at the threshold of fundamental research to industrial applications.

Scientific applications of THz radiation cover a wide range - from the study of superconductors and bio-molecules to astronomy. The development of novel techniques for detectors and sources at the forefront of science profits from the interaction of the various fields of physics and engineering.
Up to now, possibilities to generate sufficiently intense and brilliant radiation of the wavelengths in question were scarce and the region was therefore named the "THz gap". In the last years numerous promising approaches to close the gap have emerged, ranging from accelerator based sources to Quantum Cascade Lasers.

The seminar's aim was to introduce physics students and young postdocs with a focus in the field of terahertz radiation to recent developments in this vast and still growing field. In particular diploma and master students, PhD-students and young postdocs were addressed.

A wide range of terahertz sources both laboratory and accelerator based as well as detection techniques and applications of terahertz radiation were covered by experts from several institutions ranging from universities, research laboratories to industry.

In short talks and a poster session, the participants presented their own work both in scientific posters and short presentations.

Königstein-Meeting 2010
Graduated School on X-Ray Physics

Organized by:	KIT-ISS-ANKA
Date:	May 11 - 12, 17 - 21, 2010,
Venue:	KIT Campus North and Wolfach
Participants:	30

As part of a series of internal schools, the "Königsteiner Treffen 2010" was organized to be an Graduated School with invited external collaborating guests, focusing on "Coherent X-Ray Imaging". Chaired by Prof. Dr. Tilo Baumbach, it offered for about 30 participants - Diploma and Master students, PhDs and scientists of LAS / ISS - advanced training by means of various lectures related to the field of imaging. Further it provided a platform for talks by the participants themselves, opening consequent discussions to the presented topics.

The first lectures started May 11/12 at the KIT Campus Nord, while the main part of the school took place May 17-21 in a seminar house close-by the village of Wolfach, situated in the silence and natural environment of the southern German Black Forest.

Starting from the physical basics of wave field propagation and diffraction, the theoretical and methodical principles of various imaging methods were developed, covering coherence properties, X-ray imaging optics, absorption and phase contrast imaging as well as imaging in real, reciprocal and mixed spaces. Finally, the signal analysis and reconstruction algorithms for 2D and 3D data was dealt with. Altogether, a survey of the different imaging methods being used and developed at ANKA was given, allowing all participants to more extensively link their every day work to the whole framework.

Despite the tight schedule of lectures and talks, the afternoon breaks and evenings offered the possibility for unforced interdisciplinary talking and brainstorming, as well as for various off-topic team building activities as hiking and making music

Break discussions on the seminar house terrace.

Group hiking in the afternoon break.

Seminar room, break between two lectures.

ANKA Conferences, Meetings and Workshops - An Overview

Date	Organized by	Venue	Workshop Title
06. - 10.09.2009	FZK-ANKA, Karlsruhe	Hohenwart Forum Pforzheim	Joint QUASAR and THz-Groups: „Accelerator Science and Technology“
15. - 18.09.2009	FZK, European Joint Research Centre (ITU)	Congress Center Karlsruhe	ICXOM20 – The 20th International Congress on X-ray Optics and Microanalysis
29.10.2009	KIT-ISS-ANKA, Karlsruhe	KIT-ISS-ANKA, Karlsruhe	ANKA Open Day 2009
08. - 09.10.2009	KIT-ANKA and KIT-KNMF	Badnerlandhalle, Karlsruhe	1st ANKA / KNMF - Joint Users Meeting
26. - 27.11.2009	European Light Sources Activities and KIT-ANKA	KIT Campus North, Karlsruhe	First Meeting of the European Network of Light Source Communicators
19.01.2010	KIT-ANKA, Karlsruhe	KIT-ANKA, Karlsruhe	In-situ Experiments in the Material Science
23.- 24.03.2010	KIT-ISS-ANKA Department of Chemistry, University of Antwerp, Belgium	KIT Campus North	Scanning and Tomographic Micro-XRD by Means of the XRDU Software Package
18. - 21.04.2010	KIT-ANKA	Physikzentrum Bad Honnef	THz Radiation: Generation, Detection and Applications (456. WE-Heraeus Seminar)
12. - 13.05.2010 **17. - 21.05.2010**	KIT-ISS-ANKA,	Campus North and Wolfach / Black Forrest	Königstein-Meeting 2010: Graduated School on X-Ray Physics
02.07.2010	KIT-ANKA, Karlsruhe	KIT-ANKA, Karlsruhe	Committee for Research with Synchrotron Radiation - Meeting at ANKA

ANKA Seminars

Date	Speaker	Affiliation	Seminar Title
25.09.2009	Simone Di Mitri	Sincrotrone Trieste S.C.p.A., Basovizza, Trieste, Italy	The 100 nm to 4 nm FERMI@Elettra FEL Project
12.10.2009	Eberhard Goering	Max-Planck-Institut für Metallforschung, Stuttgart, Germany	A Diamond Phase Retarder used for lock in based hard X-ray magnetic circular dichroism
19.10.2009	Jens Bredenbeck	Institut für Biophysik, Johann Wolfgang Goethe Universität, Frankfurt, Germany	Multidimensional IR Spectroscopy: Chemistry and Biophysics in Real Time
30.10.2009	Yury Ivanyushenkov	Advanced Photon Source, Argonne National Laboratory, Argonne, IL, USA	Development of Superconducting Undulator for the Advanced Photon Source
04.11.2009	Daniel Schörling	TU Bergakademie Freiberg, Germany and CERN, Switzerland	Design and First Field measurements of a short model of a superconducting damping wiggler for the linear collider project CLIC
09.11.2009	Pedro F. Tavares	Visiting Scientist, ISS, KIT, Karlsruhe, Germany and Brazilian Association for Synchrotron Technology (ABTLuS), Campinas, Brasil	Accelerator Physics and Engineering Highlights at the Brazilian Synchrotron Light Source Laboratory
11.11.2009	Malte C. Kaluza	Institute of Optics and Quantum Electronics, Friedrich-Schiller-University Jena and Helmholtz-Insitute Jena, Germany	High-intensity lasers - a future alternative to conventional particle
23.11.2009	Anthony Butler	University of Otago Christchurch and University of Canterbury, New Zealand and CERN, Switzerland	MARS-CT: Multi-energy (spectroscopic) computed tomography using photon counting detectors
24.11.2009	Thomas Weiss	Stanford University, Menlo Park, CA, USA	SAXS and GiSAXS of Aligned Lipid Membrane Systems
30.11.2009	Hans Braun	PSI, Switzerland	SwissFEL – The PSI Project for a hard X-ray Free Electron Laser Facility
03.12.2009	Alexey Boubnov	University of Copenhagen, Haldor Topsøe A/S, Denmark	Structure-activity relationships of Pt/Al2O3-based diesel oxidation catalysts
13.01.2010	Charles Kitegi	Groupe Magnétisme et Insertion, Synchrotron SOLEIL, France	Development of short period high field undulators at the ESRF and SOLEIL

ANKA Seminars (continuation)

Date	Speaker	Institution	Seminar Title
18.01.2010	Guenther Rehm	Diamond, UK	Beam Diagnostics at Diamond Light Source
01.02.2010	Volker Saile	Institute for Microstructure Technology, KIT, Karlsruhe, Germany	The X-ray optics program at IMT
08.02.2010	J. Teichert	Abteilung Strahlungsquelle ELBE, Institut für Strahlenphysik, Forschungszentrum Dresden-Rossendorf, Germany	The superconducting RF photoelectron source for the ELBE accelerator at Rossendorf
22.02.2010	Stefania Pizzini	Institut Néel, CNRS and UJF, Grenoble, France	Current-induced Magnetization Dynamics in spin-valve nanostructures studied by XMCD-PEEM
04.03.2010	Giancarlo Pepponi	Fondazione Bruno Kessler, Povo, Trento, Italy	Grazing Incidence X-Ray Fluorscence Analysis and X-ray Absorption applied to characterisation of As shallow implants in Si.
08.03.2010	Enrica Chiadroni	Laboratori Nazionali di Frascati – INFN, Italy	Characterization of the THz source at SPARC
15.03.2010	Wolf-Dietrich Moeller	DESY, Hamburg, Germany	High Beta Superconducting RF Cavities for Accelerators
17.03.2010	Markus Tischer	DESY, Hamburg, Germany	Undulator Developments and Magnetic Tuning at DESY
23.04.2010	Olga Safonova	ESRF, France	Structure of catalysts under reaction conditions: Current possibilities of X-ray powder diffraction and X-ray spectroscopy
26.04.2010	Somprasong Naknaimueang	Synchrotron Light Research Institute, Thailand	The design of a electron gun grid pulse circuit for a single bunch mode syste
30.04.2010	Alexey V. Bondarenko	Novosibirsk State University, Russia	Method of beam extraction from a synchrotron by the instrumentality of multilayer coper-iron shield
10.05.2010	Karsten Meyer	Department of Chemistry & Pharmacy, University of Erlangen - Nuremberg	Carbon Dioxide Coordination, Activation, and Functionalization at Reactive Uranium Complexes

ANKA Seminars (continuation)

Date	Speaker	Institution	Seminar Title
31.05.2010	Marian Cholewa Monash	Centre for Synchrotron Science (MCSS), Monash University, Australia	New developments for the Australian Synchrotron
07.06.2010	Kostyantyn Ilyenko	Institute for Radiophysics and Electronics of NAS of Ukraine, Kharkiv, Ukraine	Hybrid planar FEL/ubitron in the magneto-resonance regime
25.06.2010	Monika Walczak	Polish Academy of Sciences, Institute of Physics, Warsaw, Poland	XAFS studies on biomaterials based on iron porphyrin structure
12.07.2010	G. Lawrence Carr	NSLS - Brookhaven National Laboratory, Upton, NY, USA	Infrared and THz Science at NSLS (and NSLS-II)
19.07.2010	Ioannis Papaphilippou and Daniel Schoerling	CERN, Switzerland	CLIC damping rings – overview ; Design of the CLIC damping rings' superconducting wigglers
30.07.2010	Andreas Koch	-	Imaging x-ray detectors in science and medical radiography - with excursions to THz imaging and x-ray generation
27.08.2010	Kunihisa Sugimoto	Japan Synchrotron Radiation Research Institute (JASRI/SPring-8), Japan	Extremely High Resolution Single Crystal Diffractometory using High Energy Synchrotron Radiation at SPring-8

Seminar Organization:
Pawel Wesolowski, Margit Costarelli

Imprint

Editors:
Dr. Pawel Wesolowski
Dr. Christine Ritschel
Dr. Ralf Hofmann
Jacqueline Heinrich
Dr. David Moss

Graphic arts, Design and Layout:
WiTec-PR, Saarbrücken
Dr. Christine Ritschel
www.witec-pr.de

Kontakt

Karlsruhe Institute of Technology (KIT)
Institute for Synchrotron Radiation

Prof. Dr. Tilo Baumbach
Director of Institute

Campus Nord
Hermann-von-Helmholtz-Platz 1
76344 Eggenstein-Leopoldshafen

ANKA User Office
Phone: +49 (0)7247 82-6188
Fax: +49 (0)7247 82-6287
E-Mail: user.office.iss@kit.edu

www.anka.iss.kit.edu

Herausgeber

Karlsruhe Institute of Technology (KIT)
Kaiserstraße 12 · 76131 Karlsruhe

Stand September 2010

www.kit.edu